https://doi.org/10.1016/j.ijsolstr.2023.112165

A fully coupled meso-scale electro-chemo-mechanical phase field method for corrosion-induced fracture in concrete

Peng Zhang[a], Jian-Guo Dai[a]*, Chandra Sekhar Das[a], Jian-Jun Zheng[b]

[a] *Department of Civil and Environmental Engineering, The Hong Kong Polytechnic University, Hong Kong, China*

[b] *School of Civil Engineering, Zhejiang University of Technology, Hangzhou 310023, China*

*Corresponding author. *E-mail address*: cejgdai@polyu.edu.hk

Abstract

Corrosion-induced concrete cover deterioration is a major factor affecting the serviceability of the reinforced concrete (RC) structures. The entire corrosion process, including mass transport, physical/chemical/electrochemical reactions, and cover cracking, occurs at the meso-scale. This paper developed a fully coupled meso-scale electro-chemo-mechanical phase field method to accurately simulate the corrosion mechanism in RC structures. The simulation begins with the mass transport process in the concrete, including the moisture, chloride ions and oxygen. When the chloride concentration at the rebar surface reaches a critical value, corrosion initiates and then propagates. A meso-scale phase field model is adopted for characterizing the corrosion-induced damage in both mortar and interfacial transition zones (ITZs). In addition, crack direction dependent diffusivity tensors are proposed to consider the influence of damage on the mass transport process. The proposed numerical method is verified by previously reported experimental results, showing the ability to conduct high-fidelity simulations of corrosion-induced fracture in RC structures. Parametric studies are carried out to investigate the effect of aggregate distribution, cover thickness, relative humidity, and temperature on the corrosion process.

Keywords: Corrosion modeling; Mass transport; Phase field method; Crack-dependent diffusivity

1. Introduction

Chloride-induced corrosion is one of the primary causes for early age deterioration of reinforced concrete (RC) structures exposed to marine environments. Generally, the embedded rebar is protected from corrosion by a passive film formed due to the highly alkaline environment in the concrete. However, as external water and chloride ions penetrate into the concrete, the passive protective layer gets destroyed, leading to corrosion of steel reinforcement. Corrosion in the RC structure is a complex process comprising physical, chemical and electrochemical reactions. As rust expands, the hoop stress in the concrete surrounding the rebar reaches the material strength, leading to tensile cracks. Subsequently, the developed cracks allow further ingress of water, chloride ions and oxygen, accelerating the corrosion process until the concrete cover is completely damaged. Corrosion is a major threat to the safety of RC structures. Therefore, in the past few decades, a considerable amount of experimental work has been carried out on the corrosion and the corresponding deterioration of the concrete cover (Andrade et al., 1993, Cabrera, 1996, Alonso et al., 1998, Castel et al., 2000, Jaffer and Hansson, 2009, Wong et al., 2010, Fischer, 2012, Ye et al., 2017, Amalia et al., 2018). However, experiments under real environmental conditions often require prolonged investigation, making them labor intensive. In this regard, a high-fidelity simulation framework can be a powerful and promising alternative.

The overall chloride-induced corrosion process comprises chloride transport, the electrochemical reactions between steel rebar and chloride ions and the resulting corrosion leading to rust formation and cracking. These crack formations lead to premature fractures in RC structures, thus expediating early age repair. Over the years, many numerical studies have been carried out to analyze the corrosion-induced fracture in RC structures. In some studies, empirical corrosion- or time-dependent corrosion models characterizing the rust distributions are used to investigate the effects of material properties or the structural factors (e.g., cover depth, cover to rebar diameter ratio and multiple rebars) on the service life estimation (Jang and Oh, 2010, Tran et al., 2011, Zhao et al., 2011, Zhang et al., 2017, Xi and Yang, 2017, Cao et al., 2013, Cao and Cheung, 2014). However, the empirical corrosion models are usually obtained from a statistical point of view. It may not be able to accurately reflect the rust distribution under specific environmental conditions. Duan et al. (2015) presented a probabilistic model to estimate the risk of chloride penetration-induced corrosion

considering the time-dependent diffusion coefficient and surface chloride concentration. Wei et al. (2021) developed a phase field model to simulate the corrosion-induced fracture of concrete with a uniform rust distribution, in which the expansion of the rust was evaluated by an empirical relationship with respect to the oxygen supply. Ožbolt et al. (2010) simulated oxygen, moisture and chloride transport processes and the interaction between the mass transport and the damage in concrete. However, the mass transport processes are not uniform and vary significantly with the changes in environmental conditions (e.g., temperature and humidity). An in-depth assessment of the temperature effect on corrosion risk was carried out by Pour-Ghaz et al. (2009a) using simulated polarization resistance tests. Chauhan and Sharma (2021) studied non-uniform corrosion in RC beams under realistic climate conditions and reported that variations in humidity and temperatures affect the crack width and pattern. Therefore, it becomes utmost important to consider environmental parameters in the corrosion model.

It is worth mentioning that most reported studies assumed concrete as a homogeneous material. This helps to reduce computational efforts when dealing with large-scale problems. However, the corrosion-induced cracks usually initiate near the rebar to concrete contact surface and are significantly affected by the aggregate distribution. Hence, an accurate simulation of the corrosion mechanism requires a meso-scale concrete model that treats the concrete as a multiple-phase material of the mortar matrix, aggregates and interfacial transition zones (ITZs). Studies using meso-scale models have been conducted to investigate the heterogenous corrosion-induced cracks in concretes with different reinforcement cases (Du et al., 2014, Chen et al., 2018, Xi et al., 2018a, Xi et al., 2018b). These studies only focused on the cracking of the concrete cover and implemented the rust expansion using empirical functions. However, based on the previous research (Qiu and Dai, 2021) the concrete's heterogeneity as well as the internal meso-scale cracks will significantly affect the mass transport process. This will subsequently affect the electrochemical reaction and the rust generation on the rebar surface. Therefore, a more comprehensive meso-scale model that can consider the entire process of the initiation and propagation of rebar corrosion is desired.

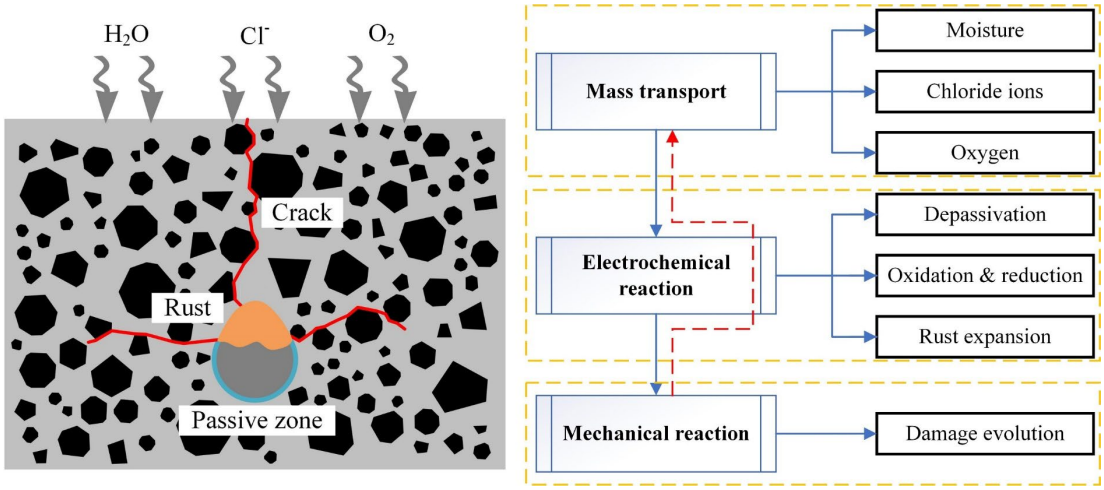

Fig. 1. Illustration and flow chart of the proposed meso-scale electro-chemo-mechanical phase field method.

The present paper proposes a comprehensive meso-scale model simulating the RC structure's entire corrosion process. As shown in Fig. 1, the simulation consists of three main parts: mass transport, electrochemical reaction and mechanical reaction. Blue and red arrows represent the interaction between the different mechanisms. The mass transport processes of moisture, chloride ions and oxygen are first considered. When the chloride concentration at the rebar surface reaches a critical value, corrosion initiates and propagates with oxygen transported through the pore solution. During this period, both micro- and macro-cell corrosion mechanisms are considered to estimate the accumulation of the rust on the rebar surface. Since the rust density is smaller than the dissolved iron, the hoop stress around the rebar will become larger with rust expansion. This will lead to damage initiation near the rebar as the hoop stress reaches the material strength. In this study, the damage of the mortar and the ITZs is modeled by a meso-scale phase field model. Phase field model is kind of non-local smeared crack model based on the Francfort-Marigo variational principle (Francfort and Marigo, 1998), in which the total potential of the damaged system is assumed as the sum of the deformation energy and the crack surface associated fracture energy, and the real displacement field and the crack set will minimize the total energy. Its ability to simulate very complex crack patterns without additional fracture criteria or crack tracking strategies makes it suitable for analysis of computational fracture problems, such as brittle fracture (Miehe et al., 2010, Ambati et al., 2015b), dynamic fracture (Bourdin et al., 2011, Borden, 2012), ductile fracture (Miehe et al., 2015, Ambati et al., 2015a), composite fracture (Zhang et al., 2019a, Quintanas-Corominas et

al., 2019, Zhang et al., 2021). In the present study, the ITZs are simulated by layers with homogenous thickness. To ensure the fracture energy conservation of the ITZs, an effective ITZ critical energy release rate is proposed for the phase field modeling. It is known that cover cracks can provide short paths for mass transport. Hence, in the present simulation by the red arrow, the influence of damage on mass transport is achieved by modified crack direction-dependent diffusivity tensors, as shown in Fig. 1. This is followed by an iteration step to consider the mass transport and electrochemical reactions based on the current damage degree, which forms a fully coupled non-mechanical and mechanical modeling framework.

The subsequent sections of the paper are constructed as follows. Section 2 deals with the details of the fully coupled electro-chemo-mechanical corrosion model as illustrated in Fig. 1 explaining the governing equations for the mass transport, electrochemical reactions and the meso-scale phase field model of fracture. The verification of the proposed electro-chemo-mechanical corrosion model and the parametric studies are conducted in section 3 and section 4, respectively. Section 5 presents the conclusions arisen from the study.

2. The fully coupled corrosion model

2.1. Mass transport

Mass transport in concrete represents a complex process. It not only varies with the concrete properties (e.g., mixture, hydration period, porosity) and the environmental factors (e.g., temperature, humidity, chloride concentration) but also involves various physical and chemical reactions with the surrounding cement hydrates. The mass transport process contains three main mechanisms, i.e., diffusion caused by concentration difference, convection caused by pore solution flow and migration caused by potential distribution in the electrolyte. Because this study focuses on the mass transport of moisture, chloride and oxygen, and the induced corrosion, diffusion and convection are assumed to be the main mechanisms in the present modeling. Moisture transport within concrete is very important for structural durability when corrosion is considered, as it is not only a key factor influencing chloride diffusion but also a transport medium for other ions and substances. The isothermal moisture transport at the macro-scale can be described by the Fick's second law, whose accurate prediction relies on two main factors, namely, the moisture capacity and

the corresponding diffusivity. The moisture capacity, which is a derivative of the equilibrium sorption isotherm, can be obtained either by empirical formulas (Van Genuchten, 1980, Xi et al., 1994a, Baroghel-Bouny, 2007, Huang et al., 2015a) or by considering the pore structure of the cement paste (Ishida et al., 2007, Maekawa, 2008). Recently, many studies have focused on modeling the water-vapor sorption isotherms taking into account the pore size distribution (Ishida et al., 2007, Maekawa, 2008, Ranaivomanana et al., 2011, Huang et al., 2015a, Pinson et al., 2015, de Burgh et al., 2016, Jiang et al., 2019), which can theoretically consider the effects of hydration degree, temperature, hysteresis, cavitation, etc. on the moisture capacity that is very complicated to be experimentally measured. Then the diffusivity, which strongly depends on the diffusion mechanisms, can be predicted either by a general expression that combines the trends of different mechanisms occurred in the pores (Saetta et al., 1993, Xi et al., 1994b, Muthulingam and Rao, 2014), or considering multi-phase (water vapor and liquid water) transport (Daian, 1988, Ishida et al., 2007, Baroghel-Bouny, 2007, Maekawa, 2008, Huang et al., 2015a). Given the water content within the concrete, the transport of other substances that depend on the concrete pore solution can be determined. Different models have been proposed to simulate the transport of chloride ions. A critical review can be referred to Shafikhani and Chidiac (2019).

It should be noted that for the sake of computational efficiency, relatively large ITZ thickness is adopted for the mechanical analysis (discussed in Section 2.3.2). However, this treatment might not apply to mass transport analysis. Hence, in the mass transport modeling the concrete is considered to be composed of impermeable aggregates and homogenized matrix (containing cement paste and ITZs (Xi and Bažant, 1999)) to eliminate the influence of the artificial bigger ITZ thickness on mass transport. The properties of the homogenized matrix will be discussed in Section 3.1.

2.1.1. Moisture transport in concrete

According to Xi et al. (1994a) the moisture transport in concrete can be described in terms of the pore relative humidity h by the mass conservation equation

$$\frac{\partial \phi_w}{\partial h}\frac{\partial h}{\partial t} - \nabla \cdot (D_h \cdot \nabla h) = 0 \tag{1}$$

where ϕ_w is the volume fraction of the pore water (m^3 of pore water/m^3 of concrete). Based on the

Brunauer-Skalny-Bodor (BSB) model of adsorption isotherm, at standard temperature and pressure, the relationship between the pore water content ϕ_w and the relative humidity h can be described by

$$\phi_w = \frac{CkV_m h}{(1-kh)[1+(C-1)kh]} \tag{2}$$

where C, k, V_m are model parameters. According to Xi et al. (1994a), for the hydration period $t_e > 5$ days and water/cement ratio $0.3 < w/c < 0.7$, the parameters can be specified as

$$V_m = \left(0.068 - \frac{0.22}{t_e}\right)(0.85 + 0.45w/c)V_{ct} \tag{3}$$

$$C = \exp\left(\frac{855}{T}\right) \tag{4}$$

$$k = \frac{(1-1/n_k)C - 1}{C-1} \tag{5}$$

and

$$n_k = \left(2.5 + \frac{15}{t_e}\right)(0.33 + 2.2w/c)N_{ct} \tag{6}$$

where T is temperature (K). V_{ct} and N_{ct} are parameters related to the type of the cement.

For cases that $t_e \leq 5$ days, one can set $t_e = 5$ days and for $w/c \leq 0.3$ and $w/c \geq 0.7$, set $w/c = 0.3$ and $w/c = 0.7$, respectively.

The diffusion coefficient (m^2/s) of the humidity, D_h is related to temperature, hydration period, and relative humidity (Saetta et al., 1993, Muthulingam and Rao, 2014) and can be described as

$$D_h = D_h^{ref} f_h(T) f_h(h) f_h(t_e) \tag{7}$$

where D_h^{ref} is reference diffusion coefficient.

The modification functions in Eq. (7) can be specified as (Bažant and Najjar, 1972)

$$f_h(T) = \exp\left[\frac{U_h}{R}\left(\frac{1}{T_{ref}} - \frac{1}{T}\right)\right] \tag{8}$$

where U_h is the activation energy of the moisture diffusion (kJ/mol). R is the gas constant (J/mol •K). T_{ref} is the reference temperature (K) at which D_h^{ref} is measured.

$$f_h(h) = \alpha_0 + \frac{1-\alpha_0}{1+(1-h)^n/(1-h_c)^n} \tag{9}$$

where α_0 is the diffusivity ratio between the minimal and maximal values of D_h. h_c is a specified humidity corresponding to the middle value of D_h and n is a model parameter.

$$f_h(t_e) = 0.3 + \sqrt{\frac{13}{t_e}} \tag{10}$$

182 describes the influence of hydration period on the moisture diffusion coefficient.

183 2.1.2. Chloride transport in concrete

184 Generally, the chlorides inside concrete exist in two forms: free chloride and bound chloride. The
185 transport of free chloride ions in non-saturated concrete can be described by (Bear and Bachmat,
186 2012, Martın-Pérez et al., 2001)

$$\frac{\partial \phi_w C_{cl}}{\partial t} = \underbrace{\nabla \cdot (D_{cl} \cdot \nabla \phi_w C_{cl})}_{\text{Diffusion}} + \underbrace{\nabla \cdot (\phi_w C_{cl} D_h \cdot \nabla h)}_{\text{Convection}} - \underbrace{\frac{\partial C_{bc}}{\partial t}}_{\text{Binding}} \tag{11}$$

187 where C_{cl} and C_{bc} are the free and bound chlorides (mol/m^3), respectively and D_{cl} is the
188 diffusion coefficient

$$D_{cl} = D_{cl}^{ref} f_{cl}(T) f_{cl}(t) f_{cl}(h) \tag{12}$$

189 where D_{cl}^{ref} is the reference diffusion coefficient measured at T_{ref}. $f_{cl}(T)$, $f_{cl}(t)$ and $f_{cl}(h)$
190 are the modification functions considering the influence of temperature, aging and relative humidity.

191 The influence of temperature on the diffusion (Bažant and Najjar, 1972) can be explained by

$$f_{cl}(T) = \exp\left[\frac{U_{cl}}{R}\left(\frac{1}{T_{ref}} - \frac{1}{T}\right)\right] \tag{13}$$

192 where U_{cl} is the activation energy of the chloride diffusion process (kJ/mol).

193 The modification function considering concrete aging (Martın-Pérez et al., 2001) can be
194 explained as

$$f_{cl}(t) = \left(\frac{t_{ref}}{t}\right)^m \tag{14}$$

195 where t_{ref} is the reference time (days) at which D_{cl}^{ref} is measured. t is the actual time in days
196 and m is an aging factor.

197 The influence of the concrete pore's relative humidity on the chloride diffusion can be
198 estimated by (Saetta et al., 1993)

$$f_{cl}(h) = \left[1 + \left(\frac{1-h}{1-h_c}\right)^4\right]^{-1} \tag{15}$$

199 where h_c is the same constant as used in Eq. (9).

The chloride binding capacity of the cement hydrates was considered using Langmuir isotherm (Luping and Nilsson, 1993, Muthulingam and Rao, 2014) and can be demonstrated as

$$C_{bc} = \frac{\alpha_L C_{cl}}{1 + \beta_L C_{cl} M_{cl}} \tag{16}$$

where α_L and β_L (m^3 of pore solution/kg) are binding constants. M_{cl} is the molar mass of chloride ion (kg/mol). Therefore, the total chloride concentration in concrete can be expressed as

$$C_{cl}^{tot} = \phi_w C_{cl} + C_{bc} \tag{17}$$

2.1.3. Oxygen transport in concrete

The equation that governs the diffusion and convection mechanisms of the oxygen can be specified as (Bear and Bachmat, 2012, Ožbolt et al., 2010)

$$\frac{\partial \phi_w C_{O_2}}{\partial t} = \underbrace{\nabla \cdot \left(D_{O_2} \cdot \nabla \phi_w C_{O_2}\right)}_{\text{Diffusion}} + \underbrace{\nabla \cdot \left(\phi_w C_{O_2} D_h \cdot \nabla h\right)}_{\text{Convection}} \tag{18}$$

where C_{O_2} is the oxygen concentration in the pore solution (mol/m^3). D_{O_2} is the effective oxygen diffusion coefficient that can be given by

$$D_{O_2} = D_{O_2}^{ref}(h) f_{O_2}(T) \tag{19}$$

where $D_{O_2}^{ref}$ is the reference oxygen diffusion coefficient measured at the reference temperature. According to the experiment results under the conditions of w/c: 0.35~0.55, T: 20~40ºC, h: 0.75~0.95 conducted by Geng et al. (2006), $D_{O_2}^{ref}$ at a temperature $T_0 = 296.15K$ can be given by

$$D_{O_2}^{ref} = 8.2236 \times 10^{-9} (w/c)^{2.346} h^{-3.247} \tag{20}$$

The temperature dependency of the oxygen diffusion can be given by Arrhenius type equation as (Pour-Ghaz et al., 2009a)

$$f_{O_2}(T) = \exp\left[\frac{U_{O_2}}{R}\left(\frac{1}{T_0} - \frac{1}{T}\right)\right] \tag{21}$$

where U_{O_2} is the activation energy of the oxygen diffusion process (kJ/mol). According to (Pour-Ghaz et al., 2009a) the activation energy of the oxygen diffusion can be given in terms of the water/cement ratio as

$$U_{O_2} = -505(w/c)^2 + 484.5 w/c - 94 \tag{22}$$

2.2. Electrochemical corrosion procedure

2.2.1. Corrosion current density

In this study, the chloride ingress into concrete is considered to be the main reason for the depassivation of the steel surface. The steel surface can be divided into active and passive zones. The active zone represents the areas of steel where the chloride concentration is higher than a critical value C_{cl}^{crt} (0.4% wt. of cement) (Cao and Cheung, 2014, Angst et al., 2009), and the remaining steel area represent the passive zone. Coupled micro- and macro-cell corrosion mechanisms are considered in the entire corrosion process (Cao et al., 2013). In order words, both anodic and cathodic reactions are considered in the active zone, while the passive zone only considers the cathodic reaction. Based on the Butler-Volmer expression, the current density of anodic reaction (iron oxidation)

$$\mathrm{Fe} \rightarrow \mathrm{Fe}^{2+} + 2e^{-} \tag{23}$$

can be described by

$$i_{Fe} = i_{Fe}^{0} \cdot \exp\left(2.303 \frac{\phi - \phi_{Fe}^{0}}{\beta_{Fe}}\right) \tag{24}$$

where ϕ is the electric potential (V). β_{Fe} is the anodic Tafel slope (V/dec). ϕ_{Fe}^{0} is the anodic equilibrium potential. i_{Fe}^{0} is the anodic exchange current density (A/m^2). Considering the influence of temperature on and the equilibrium potential the exchange density, ϕ_{Fe}^{0} and i_{Fe}^{0} can be given as (Pour-Ghaz et al., 2009a, Yu et al., 2017)

$$\phi_{Fe}^{0} = \phi_{Fe}^{0,ref} + 0.000052\left(T - T_{ref}\right) \tag{25}$$

$$i_{Fe}^{0} = i_{Fe}^{0,ref} \cdot \exp\left[\frac{\alpha_{Fe} z_{Fe} F \phi_{Fe}^{0}}{R}\left(\frac{1}{T} - \frac{1}{T_{ref}}\right)\right] \tag{26}$$

where α_{Fe} is the symmetry factor for anodic reaction. z_{Fe} is the valency of anodic reaction. F is Faraday's constant.

Similarly, the current density of the cathodic reaction (oxygen reduction)

$$\mathrm{O_2} + 2\mathrm{H_2O} + 4\mathrm{e}^{-} \rightarrow 4\mathrm{OH}^{-} \tag{27}$$

can be described by

$$i_{O_2} = i_{O_2}^{0} \cdot \frac{C_{O_2}^{st}}{C_{O_2}^{b}} \exp\left(2.303 \frac{\phi_{O_2}^{0} - \phi}{\beta_{O_2}}\right) \tag{28}$$

where $i_{O_2}^{0}$ is the cathodic exchange current density (A/m^2). $\phi_{O_2}^{0}$ is the cathodic equilibrium potential (V). β_{O_2} is the cathodic Tafel slope (V/dec). $C_{O_2}^{st}$ and $C_{O_2}^{b}$ are the oxygen concentrations at the rebar surface and concrete surface, respectively, considering the influence of oxygen

concentration polarization on the cathodic current density. Considering the influence of temperature on and the equilibrium potential the exchange density, ϕ_{Fe}^{0} and i_{Fe}^{0} can be given as (Pour-Ghaz et al., 2009a, Yu et al., 2017)

$$\phi_{O_2}^{0} = \phi_{O_2}^{0,ref} - 0.00168\left(T - T_{ref}\right) \tag{29}$$

$$i_{O_2}^{0} = i_{O_2}^{0,ref} \cdot \exp\left[\frac{\alpha_{O_2} z_{O_2} F \phi_{O_2}^{0}}{R}\left(\frac{1}{T} - \frac{1}{T_{ref}}\right)\right] \tag{30}$$

where α_{O_2} is the symmetry factor for cathodic reaction. z_{O_2} is the valency of cathodic reaction.

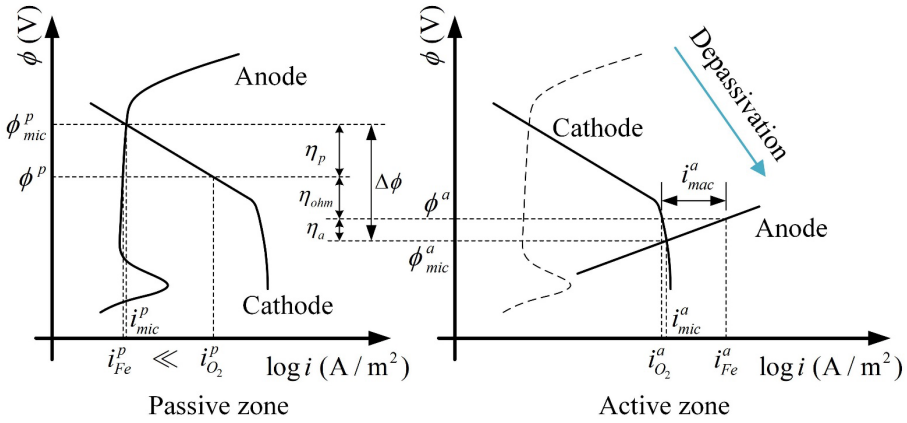

Fig. 2. Micro- and macro-cell polarization.

Fig. 2 shows the micro- and macro-cell corrosion mechanisms at the steel surface. In the passive zone the micro-cell potential ϕ_{mic}^{p} and the corresponding current density i_{mic}^{p} can be obtained by the intersection point of the anodic and the cathodic polarization curves. With the increase of the chloride concentration, the anodic polarization curve moves downwards as shown in Fig. 2 and the corresponding area turns into the active zone. The corresponding micro-cell potential and current density are ϕ_{mic}^{a} and i_{mic}^{a}. It can be seen that the passive zone has a bigger micro-cell potential ($\phi_{mic}^{p} > \phi_{mic}^{a}$), while the corresponding micro-cell current density is much smaller than that of the active zone, i.e., $i_{mic}^{p} \ll i_{mic}^{a}$.

As shown in Fig. 2, rebar (as conductor) and concrete pore solution (as electrolyte) also form a macro-cell corrosion system. The macro-cell corrosion may cause the decrease of the potential at the passive zone $\eta_p = \phi_{mic}^{p} - \phi^{p}$. The corresponding anodic and cathodic current densities are i_{Fe}^{p} and $i_{O_2}^{p}$. It is worth noting that i_{Fe}^{p} is usually much smaller than $i_{O_2}^{p}$, i.e., $i_{Fe}^{p} \ll i_{O_2}^{p}$, which has

$$i_{Fe}^{p} \cong i_{mic}^{p} \cong 0 \tag{31}$$

Thus, the total current density in the passive zone can be given as

$$i_{total}^{p} = i_{mac}^{p} + i_{mic}^{p} \cong -i_{O_2}^{p} \tag{32}$$

In the active zone the polarization may cause the increase of the potential $\eta_a = \phi^a - \phi_{mic}^a$. The corresponding macro-cell anodic and cathodic current densities are i_{Fe}^a and $i_{O_2}^a$, respectively. Therefore, the total macro-cell corrosion density in the active zone can be given as

$$i_{mac}^{a} = i_{Fe}^{a} - i_{O_2}^{a} \tag{33}$$

The potential difference η_{ohm} that is generated from the macro-cell corrosion current circulating through concrete between the active and passive zones is termed as the ohmic drop. Accordingly, the total current density (corrosion current density) in the active zone can be obtained as (Cao et al., 2013)

$$i_{corr}^{a} = i_{mac}^{a} + i_{mic}^{a} \cong i_{Fe}^{a} \tag{34}$$

2.2.2. Electrical potential distribution

The porous concrete with pore solution can be regarded as a conductor. Based on Ohm's law, a Laplace equation can be adopted to describe the electrical potential distribution in the concrete (Ožbolt et al., 2011, Cao et al., 2013)

$$\nabla \cdot \left(\frac{1}{\rho}\nabla\phi\right) = 0 \tag{35}$$

where ϕ is the electrical potential (V). ρ is the effective resistivity ($\Omega \cdot \mathrm{m}$). Accordingly, the current flux can be specified as

$$i = -\frac{1}{\rho}\nabla\phi \tag{36}$$

The temperature dependency of the resistivity can be given by (Pour-Ghaz et al., 2009b)

$$\rho = \rho_{ref} \cdot \exp\left[\frac{U_\rho}{R}\left(\frac{1}{T} - \frac{1}{T_{ref}}\right)\right] \tag{37}$$

where U_ρ is the activation energy (kJ/mol), which can be given by (Pour-Ghaz et al., 2009b)

$$U_\rho = \frac{26.753349}{1 - 4.3362256 \times \exp(-5.2488563 \cdot h)} \tag{38}$$

ρ_{ref} is the reference resistivity. In the present study, the electrical conductivity, which is $1/\rho_{ref}$ ($\Omega^{-1} \cdot \mathrm{m}^{-1}$), is adopted (Ožbolt et al., 2011). The electrical conductivities for $w/c = 0.4$ and $w/c = 0.7$ are given in Tab. 1. A linear interpolation is used to calculate the values corresponding to the water/cement ratios between 0.4 and 0.7.

Tab. 1. Electric conductivity of concrete with different degrees of saturation(Ožbolt et al., 2011).

Saturation (%)	35	40	45	50	55	60	65	70	75	80	85	90	95
$w/c = 0.4$ (10^{-3})	0.01	0.03	0.07	0.20	0.25	0.53	0.75	1.0	2.0	6.0	10.0	11.2	12.5
$w/c = 0.7$ (10^{-3})	0.50	1.00	1.81	2.75	3.00	4.28	8.70	9.52	10.5	11.5	12.5	13.5	14.2

In electromechanical analysis, the current densities at the electrode surface can serve as boundary conditions of the Laplace equation (Eq. (35)). Hence, the total flux passing through the electrolyte (concrete) should be equal to the macro-cell current density at the steel surface, which is

$$i_{mac} = -\boldsymbol{n} \cdot \left(\frac{1}{\rho}\nabla\phi\right)\Big|_{\text{steel surface}} \tag{39}$$

where $\boldsymbol{n}$ is the unit vector normal to the rebar surface. According to Eqs. (31)-(33), the above boundary condition can be rewritten as

$$i_{Fe}^{a} - i_{O_2}^{a} = -\boldsymbol{n} \cdot \left(\frac{1}{\rho}\nabla\phi\right), \qquad \text{in active zone} \tag{40}$$

$$-i_{O_2}^{p} = -\boldsymbol{n} \cdot \left(\frac{1}{\rho}\nabla\phi\right), \qquad \text{in passive zone} \tag{41}$$

To numerically describe the propagation of the active zone, a modified anodic Tafel slope is adopted as

$$\beta_{Fe} = \begin{cases} \beta_{Fe} & \text{active zone where } \phi_w C_{cl} \geq C_{cl}^{crt} \\ \infty & \text{passive zone where } \phi_w C_{cl} < C_{cl}^{crt} \end{cases} \tag{42}$$

2.2.3. Oxygen consumption

During the electrochemical corrosion process, the cathodic reaction occurs in active and passive zones. In this study, the cathodic reaction is assumed to be the only mechanism that consumes oxygen. Therefore, according to Faraday's law, the relationship between the oxygen flux and the cathodic current density at the steel surface can be given by

$$i_{O_2} = -z_{O_2} F \cdot \boldsymbol{J}_{O_2}, \qquad \text{at steel surface} \tag{43}$$

where $z_{O_2} = 4$ is the valency of the cathodic reaction. F is Faraday's constant. $\boldsymbol{J}_{O_2}$ is the oxygen flux. According to Fick's law, $\boldsymbol{J}_{O_2}$ can be specified as

$$\boldsymbol{J}_{O_2} = -\boldsymbol{n} \cdot D_{O_2} \nabla C_{O_2}^{st}, \qquad \text{at steel surface} \tag{44}$$

2.2.4. Iron dissolution and rust generation

The corrosion of the steel bar in the concrete is a long-term process. The dissolution of the steel bar

is caused by the anodic reaction. According to Faraday's law, the corrosion depth of the steel surface can be described by the corrosion current density as (Cao et al., 2013)

$$\frac{\partial p(\boldsymbol{x},t)}{\partial t} = \frac{M_{Fe}}{z_{Fe}F\rho_{Fe}} i_{corr}^{a}(\boldsymbol{x},t), \qquad \text{at active zone} \tag{45}$$

where $p(\boldsymbol{x},t)$ is the corrosion depth of the steel surface. M_{Fe} is the molar mass of iron. z_{Fe} is the valency of anodic reaction. ρ_{Fe} is the density of the rebar.

As the reaction process, the rust product will form and accumulate around the steel surface. The density of the insoluble rust product is larger than that of the iron. Therefore, the rust-steel system will expand in volume. The volume expansion along the rebar radius direction (Suda et al., 1993, Cao et al., 2013) can be given by

$$u_{rust}(\boldsymbol{x},t) = (r_v - 1)\cdot p(\boldsymbol{x},t), \qquad \text{at active zone} \tag{46}$$

where r_v is the volumetric expansion ratio.

2.3. Meso-scale Phase field model for corrosion-induced fracture

2.3.1. Phase field model

Based on (Francfort and Marigo, 1998) the potential energy of the system can be given by

$$\mathfrak{E} = \mathfrak{E}_e + \mathfrak{E}_f - \mathfrak{E}_{ext}, \qquad \text{in } \Omega \tag{47}$$

where $\Omega \subset \mathbb{R}^3$ is the considered domain. $\mathfrak{E}_e$ is the deformation energy, which can be specified by

$$\mathfrak{E}_e = \int_{\Omega} \omega_d(d)\cdot\psi_e(\boldsymbol{\epsilon})\,\mathrm{d}V, \qquad \text{in } \Omega \tag{48}$$

where $\boldsymbol{\epsilon}$ is the strain tensor and $\psi_e(\boldsymbol{\epsilon})$ is the corresponding deformation energy density. $d(\boldsymbol{x})$ is the phase field value at point $\boldsymbol{x}$, in which $d = 0$ and $d = 1$ represent intact and totally damaged material states. $\omega_d(d)$ is the degradation function characterizing the damage degree of the material. In this study, the parametric degradation function proposed by Wu (2017) is adopted, which is

$$\omega_d(d) = \frac{(1-d)^2}{(1-d)^2 + a_1 d + a_1 a_2 d^2} \tag{49}$$

in which a_1 and a_2 are parameters that are related to different stress softening relationships. Here, a widely adopted linear softening relationship is adopted

$$a_1 = \frac{4EG_c}{c_0 l_0 Y_t^2}, \quad \text{and} \quad a_2 = -0.5 \tag{50}$$

where E is the Young's modulus. Y_t is the material strength.

The fracture energy $\mathfrak{E}_f$ can be specified by

$$\mathfrak{E}_f = \int_\Omega G_c \cdot \gamma_d(d, \nabla d)\, \mathrm{d}V, \qquad \text{in } \Omega \tag{51}$$

where G_c is the critical energy release rate. $\gamma(d, \nabla d)$ is the crack surface density function, which can be given by (Bourdin et al., 2000)

$$\gamma_d(d, \nabla d) = \frac{1}{c_0}\left[\frac{1}{l_0}\alpha(d) + l_0 \nabla d \cdot \nabla d\right] \tag{52}$$

where l_0 is the phase field internal length scale used to characterize the width of the smeared crack. c_0 is a model parameter, which is

$$c_0 = \int_0^1 \alpha(s)\, \mathrm{d}s \tag{53}$$

where $\alpha(d)$ is the crack geometry function. In this study, a polynomial form (Wu, 2017) is adopted as

$$\alpha(d) = 2d - d^2 \tag{54}$$

The external energy $\mathfrak{E}_{ext}$ can be specified by

$$\mathfrak{E}_f = \int_\Omega \bar{\boldsymbol{b}} \cdot \boldsymbol{u}\, \mathrm{d}V + \int_{\Gamma_t} \bar{\boldsymbol{t}} \cdot \boldsymbol{u}\, \mathrm{d}S \tag{55}$$

where $\bar{\boldsymbol{b}} \in \mathbb{R}^3$ is the body force. $\bar{\boldsymbol{t}} \in \mathbb{R}^2$ is the boundary force at $\Gamma_t \subset \mathbb{R}^2$.

According to the Francfort-Marigo variational principle (Francfort and Marigo, 1998), the governing equations and boundary conditions can be obtained as

$$\nabla \cdot [\omega_d(d)\boldsymbol{\sigma}] + \bar{\boldsymbol{b}} = \boldsymbol{0}, \qquad \text{in } \Omega \tag{56}$$

$$\frac{G_c}{c_0 l_0}[\alpha'(d) - 2l_0 \Delta d] = -\omega_d'(d)\mathcal{H}_t, \qquad \text{in } \Omega \tag{57}$$

$$\omega_d(d)\boldsymbol{\sigma} \cdot \boldsymbol{n} = \bar{\boldsymbol{t}}, \qquad \text{on } \Gamma_t \tag{58}$$

$$\nabla d \cdot \boldsymbol{n} = \boldsymbol{0}, \qquad \text{on } \Gamma \tag{59}$$

where $\mathcal{H}_t$ is a solution dependent variable used to prevent self-healing of the damage (Miehe et al., 2010), which can be specified by

$$\mathcal{H}_t = \max_{\tau \in [0,t]} \{\psi_e(\boldsymbol{\epsilon}, \tau)\} \tag{60}$$

2.3.2. Meso-scale phase field model

Concrete is a multi-phase material containing aggregates, mortar and the ITZs between them. Generally, the computational fracture modeling of concrete is usually conducted in two length scales: computational mechanics (macro-scale) and computational mesomechanics (meso-scale). In macro-scale modeling, concrete is treated as a homogenous material, with effective material properties

obtained from experimental tests or numerical homogenization methods. The heterogeneity of the concrete is not considered at this scale, so it is very suitable for large-scale modellings. However, for corrosion-induced fracture the damage usually occurs within the concrete cover, whose thickness is usually $10\text{mm} - 50\text{mm}$ and is comparable to the diameter of the coarse aggregate (usually $2.4\text{mm} - 19.05\text{mm}$). The heterogeneity of the concrete cover due to the presence of aggregates will have significant influences on both the damage and mass transport processes. Therefore, in this study, a meso-scale model, which can explicitly consider different phases, is adopted to simulate the entire corrosion process of the reinforced concrete accurately.

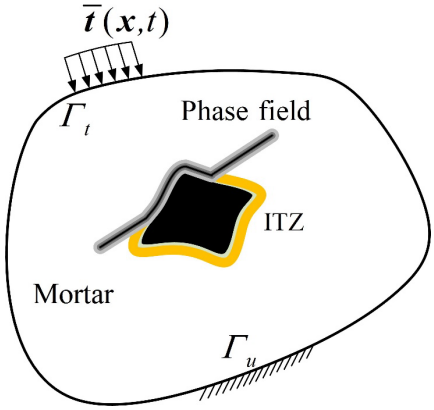

Fig. 3 Meso-scale phase field model for concrete cracking.

Fig. 3 shows the meso-scale phase field model for concrete cracking. In the model, the mortar, the aggregate and the ITZs are regarded as homogenous isotropic materials. Accurate modeling of the ITZ damage poses a challenge because of the complex topology and extremely thin thickness (usually tens of micrometers). However, recent investigations show that in the fracture modeling, an approximate ITZ thickness of $0.1\text{mm} - 1\text{mm}$ can be adopted to characterize the damage behavior in the meso-scale model and will not significantly affect the fracture behavior of the structure (Šavija et al., 2013, Du et al., 2014, Huang et al., 2015b, Zhou et al., 2017, Zhang et al., 2019b, Hu et al., 2022). In the present study, the ITZ thickness is assumed to be 0.5mm based on previous studies (Hu et al., 2022). Then the ITZ damage and mortar cracking are characterized using a unified phase field modeling framework. To further reduce the computational effort, we assume that the smeared crack width can be wider than the ITZ. Then, an effective ITZ critical energy release rate $\tilde{G}_i$ is proposed to prevent the non-conversation of the ITZ fracture energy that is caused

by the inconsistency between the smeared crack width and ITZ thickness. According to the fracture energy conservation $\tilde{G}_i$ can be obtained by

$$G_i = \int_0^{l_z} \tilde{G}_i \cdot \gamma_d(d, \nabla d)\, \mathrm{d}x + \int_{l_z}^{D_c} G_m \cdot \gamma_d(d, \nabla d)\, \mathrm{d}x \tag{61}$$

where G_i and G_m are the critical energy release rates of the ITZ and the mortar, respectively. l_z is the thickness of the ITZ. D_c is the half width of the smeared crack and d is the phase field distribution along the ITZ thickness direction. According to the analytical solution of the 1-D phase field model, D_c and d can be given as (Wu, 2017)

$$D_c = \frac{\pi}{2} \cdot l_0 \tag{62}$$

$$d = 1 - \sin\left(\frac{x}{l_0}\right) \tag{63}$$

Substituting Eqs. (62) and (63) into Eq. (61), the effective critical energy release rate of the ITZ can be obtained as

$$\tilde{G}_i = \frac{[2G_i c_0 - G_m c_0 + G_m \sin(2l_z/l_0)]l_0 + 2G_m l_z}{\sin(2l_z/l_0)\, l_0 + 2G_m l_z} \tag{64}$$

2.3.3. Influence of damage on mass transport

In the past few decades, considerable work has been done to investigate the influence of concrete damage on the mass transport process. Experimental observations show that surface cracks increase the ingress of different substances into concrete (Aldea et al., 2000, Wang et al., 1997). Based on the results, Ožbolt et al. (2010) tried to propose the moisture diffusion coefficient of the damaged region using the undamaged diffusion coefficient multiplied by a normalized permeability coefficient and validated it as shown in Fig. 4. This modified moisture diffusion coefficient is adopted in the present study and is represented as

$$D_h^c = \alpha \cdot D_h \tag{65}$$

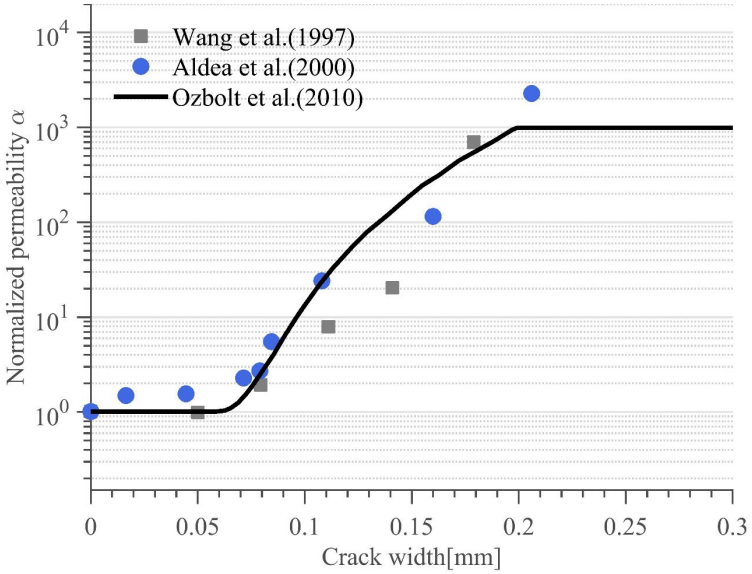

Fig. 4. The relationship between the crack width and the normalized permeability.

For oxygen diffusion, the coefficient can be drastically increased with the increasing of the crack width. According to Cao et al. (2013), the flow of oxygen through cracks can be described by Poiseuille's law for laminar flow. Therefore, the oxygen diffusion coefficient within cracks can be given by

$$D_{O_2}^c = D_{O_2} \cdot \left(\frac{[\![u]\!]}{[\![u]\!]_c} \right)^3, \quad \text{for } [\![u]\!] > [\![u]\!]_c \tag{66}$$

where $[\![u]\!]$ is the crack width. $[\![u]\!]_c$ is a critical crack width beyond which the effect of damage on diffusivity should be considered.

Djerbi et al. (2008) investigated the effect of transverse crack on the chloride diffusion. Based on the experimental results, they found that the crack width has a significant influence on the chloride diffusivity, which can be given by

$$D_{cl}^c = \begin{cases} 2 \times 10^{-11} [\![u]\!] - 4 \times 10^{-10}, & \text{for } 30\mu\text{m} \le [\![u]\!] \le 80\mu\text{m} \\ 14 \times 10^{-10}, & \text{for } [\![u]\!] > 80\mu\text{m} \end{cases} \tag{67}$$

Modified diffusion coefficients in Eqs. (65)-(67) show that the diffusivity is highly related to the crack width. Theoretically, the modified diffusion coefficient within the cracks should be explicitly considered in the modeling with the moving crack surfaces as boundary conditions. However, even for very simple crack patterns, it will be a very complicated task. Therefore, in the present study, the modified coefficients are implicitly considered by using an effective crack width specified by

$$[\![u]\!]_{eff} = \langle \epsilon_1 \rangle_+ \cdot \omega_d(d) h_e \tag{68}$$

where the bracket operator is defined as

$$\langle \epsilon_1 \rangle_+ = \frac{\epsilon_1 + |\epsilon_1|}{2} \tag{69}$$

in which ϵ_1 is the first principal strain. h_e is the characteristic element length. However, the effective crack width in Eq. (68) cannot be directly used in Eqs. (65)-(67). Because the increase of the diffusion coefficient only occurs within the cracks. Direct utilization of Eq. (68) will implement a modified diffusivity to the whole element, which will cause a significant element size sensitivity and inconsistency with the experimental observations. Therefore, to correctly consider the modified diffusivity, we assume that the diffusion coefficient in the damaged elements consists of two parts: the coefficient of the intact concrete and the increased coefficient due to damage. Thus, the modified diffusion coefficient can be given by

$$\widetilde{D}_X^c = D_X + \Delta D_X^c \tag{70}$$

where X represents the considered substances, i.e., moisture, chloride and oxygen. ΔD_X^c is the increased coefficient attributed to the damage, which is given by

$$\Delta D_X^c = \frac{D_X^c\left([\![u]\!]_{eff}\right) \cdot [\![u]\!]_{eff}}{h_e} = D_X^c\left([\![u]\!]_{eff}\right) \cdot \omega_d(d)\langle \epsilon_1 \rangle_+ \tag{71}$$

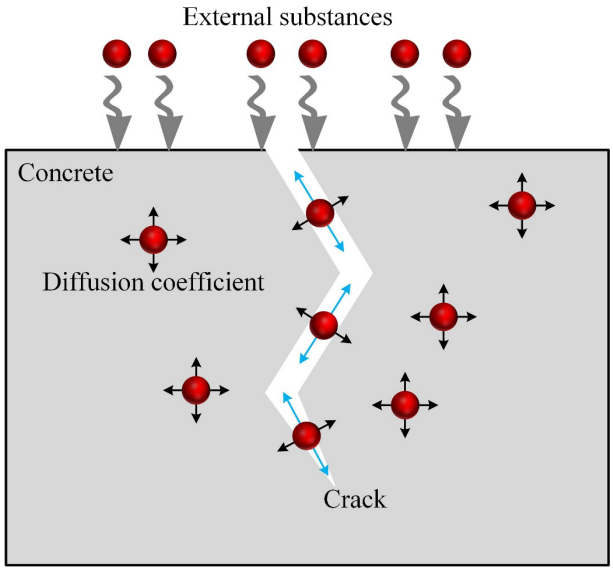

Fig. 5. Substance diffusion coefficient in cracked concrete.

Fig. 5 illustrates the transport process of the substances within cracked concrete. External substances and the diffusion coefficient are denoted by the red balls and the attached arrows. The figure shows that the diffusion coefficient is isotropic in the intact zone. However, the diffusion

coefficient becomes anisotropic for substances transported through cracks. For direction along the crack surface, the coefficient is significantly increased, which is described by Eq. (71). For direction perpendicular to the crack surface, the coefficient remains the same as that in the intact zones. Hence, to achieve this crack direction dependent diffusion coefficient, we propose an anisotropic coefficient tensor as

$$\widetilde{\boldsymbol{D}}_X^c = D_X \cdot \boldsymbol{I} + \Delta D_X^c \cdot (\boldsymbol{I} - \boldsymbol{n_1} \otimes \boldsymbol{n_1}) \tag{72}$$

where $\boldsymbol{I}$ is the second-order unit tensor. $\boldsymbol{n_1}$ is the unit vector perpendicular to the crack surface, which can be specified by

$$\boldsymbol{n}_1 = \frac{\nabla d}{\|\nabla d\|} \tag{73}$$

In order to clearly demonstrate the influence of Eq. (72) on the diffusion process, we consider a simple steady state of substance X diffusion, whose governing equation can be specified by

$$\nabla \cdot (D_X \nabla C_X) = 0 \tag{74}$$

in which D_X is the isotropic diffusion coefficient. Assuming a zero-flux boundary condition W_X, Eq. (74) can be considered as a Euler equation of the following variational principle

$$C_X = \mathrm{Arg}\left\{\inf_{W_X} I_X(C_X)\right\} \tag{75}$$

in which $I_X(C_X)$ is a kind of generalized free energy of diffusion. One of the possible forms of $I_X(C_X)$ that satisfies Eqs. (74) and (75) can be given by

$$I_X(C_X) = \frac{1}{2}\int_\Omega D_X \cdot \|\nabla C_X\|^2 \,\mathrm{d}V \tag{76}$$

According to Eqs. (72) and (76), the generalized free energy of diffusion at the damaged zone can be given by

$$I_X^c(C_X) = \frac{1}{2}\int_\Omega \widetilde{\boldsymbol{D}}_X^c : \nabla C_X \otimes \nabla C_X \,\mathrm{d}V \tag{77}$$

Substituting Eq. (72) into Eq. (77), it has

$$I_X^c(C_X) = \frac{1}{2}\int_\Omega \left[D_X + \Delta D_X^c \cdot \sin^2\langle \boldsymbol{n}_1, \nabla C_X\rangle\right] \cdot \|\nabla C_X\|^2 \,\mathrm{d}V \tag{78}$$

By mimicking Eq. (76), an effective diffusion coefficient at the cracked zone can be given as

$$D_X^{eff} = D_X + \Delta D_X^c \cdot \sin^2\langle \boldsymbol{n}_1, \nabla C_X\rangle \tag{79}$$

Through the above derivations, it can be seen that Eq. (79) is actually equivalent to Eq. (72). Let θ denote the angle between the crack direction and the gradient of concentration of X. The relationship between the effective diffusion coefficient and θ is depicted in Fig. 6. In the figure,

lines with different colors represent different damage degrees, i.e., crack widths. It can be seen that for the intact zones ($\omega_d = 1$) the diffusion coefficient is isotropic and equal to D_X. For the damaged zones, the coefficients along and perpendicular to the crack direction are increased and unchanged, respectively. In addition, the diffusion coefficient along the crack direction increases with the increase in the crack width, which is consistent with the experimental observations (Djerbi et al., 2008).

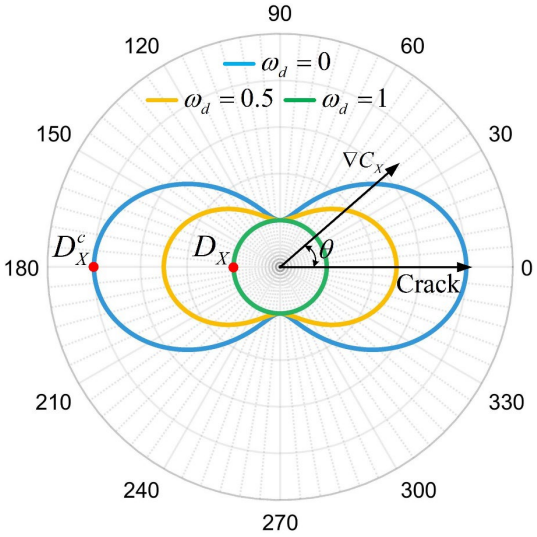

Fig. 6. Crack direction dependent diffusion coefficient.

3. Verification

3.1. Specimen and material properties

The proposed meso-scale electro-chemo-mechanical model was verified by an experiment conducted by Ye et al. (2017). The geometry and boundary conditions of the experiment program are shown in Fig. 7. Four rebars of diameter 12 mm are embedded in the corners of the specimen and denoted as C10, C15, C20 and C25 based on their distances from the concrete surfaces. The specimens were placed in an environmental chamber with 33°C and 80% relative humidity. The surface chloride concentration $C_{cl}^{s}(t) = 0.12t^{0.54}$ suggested by (Muthulingam and Rao, 2014) is adopted. The oxygen concentration at the concrete surface is assumed to be 0.268 mol/m^3 (Cao et al., 2013). The material properties for mass transport used by Muthulingam and Rao (2014) and Ožbolt et al. (2010) shown in Tab. 2 are adopted. The electrochemical properties for corrosion used by Cao et al. (2013) and Zhu and Zi (2017) are adopted as given in Tab. 3.

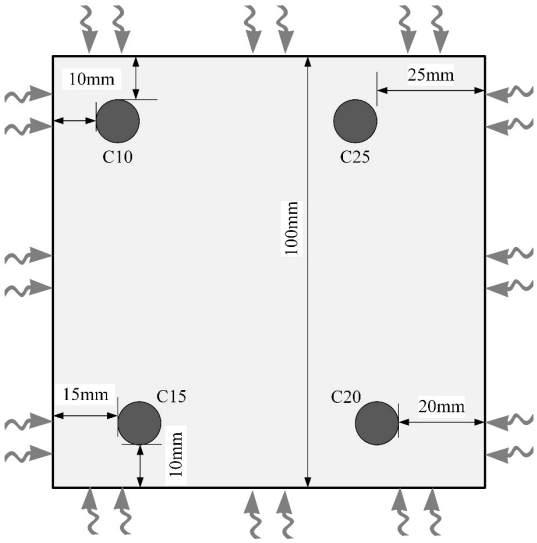

Fig. 7. Geometry of the specimen and rebars.

Tab. 2. Properties for mass transport. (Muthulingam and Rao, 2014, Ožbolt et al., 2010)

property	value
Reference moisture diffusion coefficient D_h^{ref}	2×10^{-11} m^2/s
Moisture diffusion activation energy U_h	20.3 kJ/mol
Gas constant R	8.31 J/mol
Reference temperature T_{ref}	296 K
Specified relative humidity h_c	0.75
Moisture diffusivity ratio α_0	0.05
Model parameter for humidity n	10
Hydration period t_e	28 days
Water/cement ratio w/c	0.5
Reference chloride diffusion coefficient D_{cl}^{ref}	3.4×10^{-12} m^2/s
Binding constant α_L	0.39
Binding constant β_L	0.07 m^3/kg
Molar mass of chloride ion M_{cl}	35.5 g/mol
Chloride diffusion activation energy U_{cl}	44.6 kJ/mol
Reference time t_{ref}	28 days
Aging factor m	0.15

Tab. 3. Properties for electrochemical corrosion. (Cao et al., 2013, Zhu and Zi, 2017)

Property	Value
Anodic exchange current i_{Fe}^0	3×10^{-4} A/m^2
Cathodic exchange current $i_{O_2}^0$	1×10^{-5} A/m^2
Anodic equilibrium potential ϕ_{Fe}^0	-0.78 V
Cathodic equilibrium potential $\phi_{O_2}^0$	0.16 V
Anodic Tafel slope β_{Fe}	0.09 V/dec

Cathodic Tafel slope β_{O_2}	0.18 V/dec
Faraday's constant F	96486.7
Volumetric expansion ratio r_v	2.96
Molar mass of iron M_{Fe}	55.845 g/mol
Density of rebar ρ_{Fe}	7.87 g/cm^3

462

463 For normal strength concrete, the Young's modulus of the coarse aggregate can be estimated
464 according to the Code (2005) as

$$E_a = 22\left(\frac{f_a}{10}\right)^{0.3} \tag{80}$$

465 where f_a is the corresponding cubic compressive strength. According to (Contrafatto et al., 2016,
466 Li et al., 2021), f_a can be set to be 122.63 MPa.

467 According to Lu et al. (2005) the Young's modulus of the homogenized concrete E_c can be
468 estimated by

$$E_c = \frac{100}{2.2 + 34.74/f_c} \tag{81}$$

469 where f_c is the cubic compressive strength of the concrete. In the experiment, this parameter was
470 measured by Ye et al. (2017) as $f_c = 42.5$ MPa. Then, by using the Mori-Tanaka homogenization
471 theory (Mori and Tanaka, 1973, Li et al., 2021), the Young's modulus of the mortar E_m can be
472 estimated by

$$E_c = E_m + \frac{V_a(E_a - E_m)}{1 + (1 - V_a)g_m} \tag{82}$$

473 in which V_a is the aggregate volume fraction. In the present study, a place and take aggregate
474 generation algorithm (Xi et al., 2018b) is adopted, and a volume fraction about 0.37~0.4 is adopted
475 for all the simulations. g_m is a parameter, which can be specified by

$$g_m = \frac{E_a - E_m}{E_m + 4\mu_m/3} \tag{83}$$

476 where

$$\mu_m = \frac{E_m}{2(1 + v_m)} \tag{84}$$

477 where v_m is the Poisson's ratio of the mortar. In the present study, the Poisson's ratio 0.2 is used
478 for the homogenized concrete, the mortar and the aggregate (Huang et al., 2016, Li et al., 2021).

479 The corrosion-induced fracture is modeled by the meso-scale phase field model introduced in
480 section 2.3. As the model explicitly considers different phases, the corresponding fracture properties

such as material strength and critical energy release rate, are used in the analysis. According to Nagai et al. (2005), the tensile strength Y_m and the tensile critical energy release rate G_m of the mortar can be estimated by

$$Y_m = 1.4 \cdot \ln\left(f_m^{'}\right) - 1.5 \tag{85}$$

$$G_m = (0.0469 d_a^2 - 0.5 d_a + 26)\left(\frac{f_m^{'}}{10}\right)^{0.7} \tag{86}$$

where the parameter $d_a = 2.36\text{mm}$ (Li et al., 2021). $f_m^{'}$ is the cylinder compressive strength of the mortar that can be estimated by (Sideris et al., 2004)

$$f_m^{'} = \frac{E_m - 12.4147}{0.2964} \tag{87}$$

For ITZ damage, the tensile strength Y_i can be estimated by (Nagai et al., 2005)

$$Y_i = -1.44 C_w + 2.3 \tag{88}$$

where

$$C_w = \frac{1}{0.047 f_m^{'} + 0.5} \tag{89}$$

Finally, based on previous studies (López et al., 2008, Huang et al., 2016), the ITZ tensile critical energy release rate is set to be half that of the mortar, i.e., $G_i = 0.5 G_m$.

According to Xi and Bažant (1999) when considering aggregate volume fraction less than 50%, the matrix can be assumed to be composed of bulk cement past and ITZs, and the properties of the matrix should be considered as a function of the aggregate content. As suggested by Xi and Bažant (1999) the relationship between the diffusivities of the concrete D_c and the matrix (i.e., cement paste and ITZs) D_m can be expressed as (Christensen, 1979)

$$D_c = D_m \frac{2(1 - V_a)}{2 + V_a} \tag{90}$$

In the present simulation, this equation is used to evaluate the diffusion coefficient of the matrix (i.e., mortar and ITZs). It is because that for mechanical analysis, relatively large ITZ thickness is adopted to reduce the computation efforts as discussed in Section 2.3.2. However, this strategy might not apply to diffusion analysis. Eq. (90) treating cement paste and ITZs as a homogenized matrix, makes it possible for the present simulation to adopt a larger ITZ thickness as well as consider the influence of the ITZs on the diffusivity in a more reasonable way. This equation is used for all the substances considered in the mass transport process.

3.2. Results

As non-uniform rust expands at the rebar surfaces, the predicted crack patterns are depicted in Fig. 8. It can be seen that all cracks are concentrated near the rebars, and the cracks tend to develop along the ITZs, which are the weakest regions in the concrete domain. The coarse aggregates near the surface significantly affect the surface's crack position and propagation. This can be attributed to the comparable sizes of the coarse aggregates and the concrete cover thickness. In summary, the surface crack tends to initiate near bigger aggregates, then propagates along the ITZs and the mortar between them, creating an additional path for mass transport, which will surely increase the corrosion process. The corner spalling phenomenon observed in the experiment conducted by Fischer (2012) is accurately predicted by the present simulation, as shown in Fig. 8. It can be seen that corner rebars, equidistant from the upper and the left concrete surfaces, form a scissors-like crack pattern: two cracks perpendicular to the surfaces and two inline cracks inclined to the surfaces. Additionally, it can be observed that the cracks between two rebars tend to merge leading to concrete cover delamination.

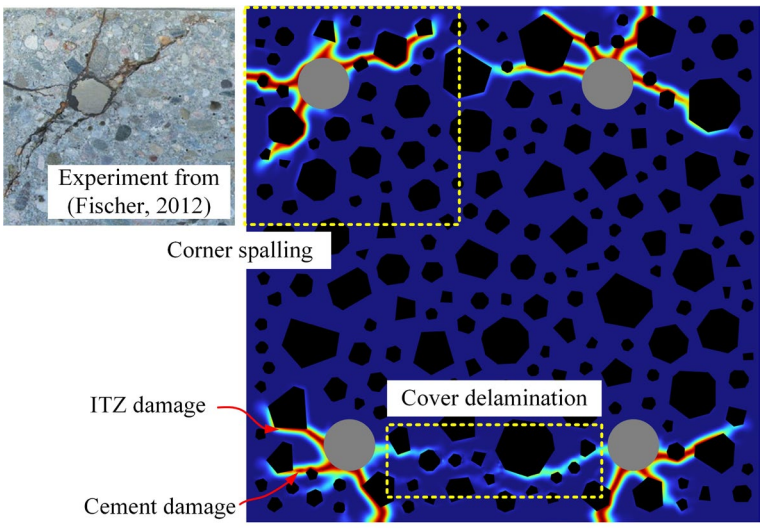

Fig. 8. Predicted crack patterns and comparison with the experimental corner spalling.

Fig. 9 shows the relationships between the steel loss ratio, defined as the ratio between the loss cross-sectional area of the rebar and the original area, and the surface crack width for different rebar locations. These are compared with the experimental results from Ye et al. (2017). It is noteworthy that the experiment was conducted in an accelerated timeframe, so in this section, only the steel loss

ratio is considered instead of the corrosion time. Fig. 9 shows that for all four rebars, the surface crack widths increase with the corrosion propagation, and the predicted results agree well with the experimental observations. In addition, the steel loss ratio versus crack width curves for C15, C20 and C25 show clear jumps at different steel loss ratios. This is caused by the sudden damage of the surface cracks, especially when relatively large aggregates exist near the concrete surface.

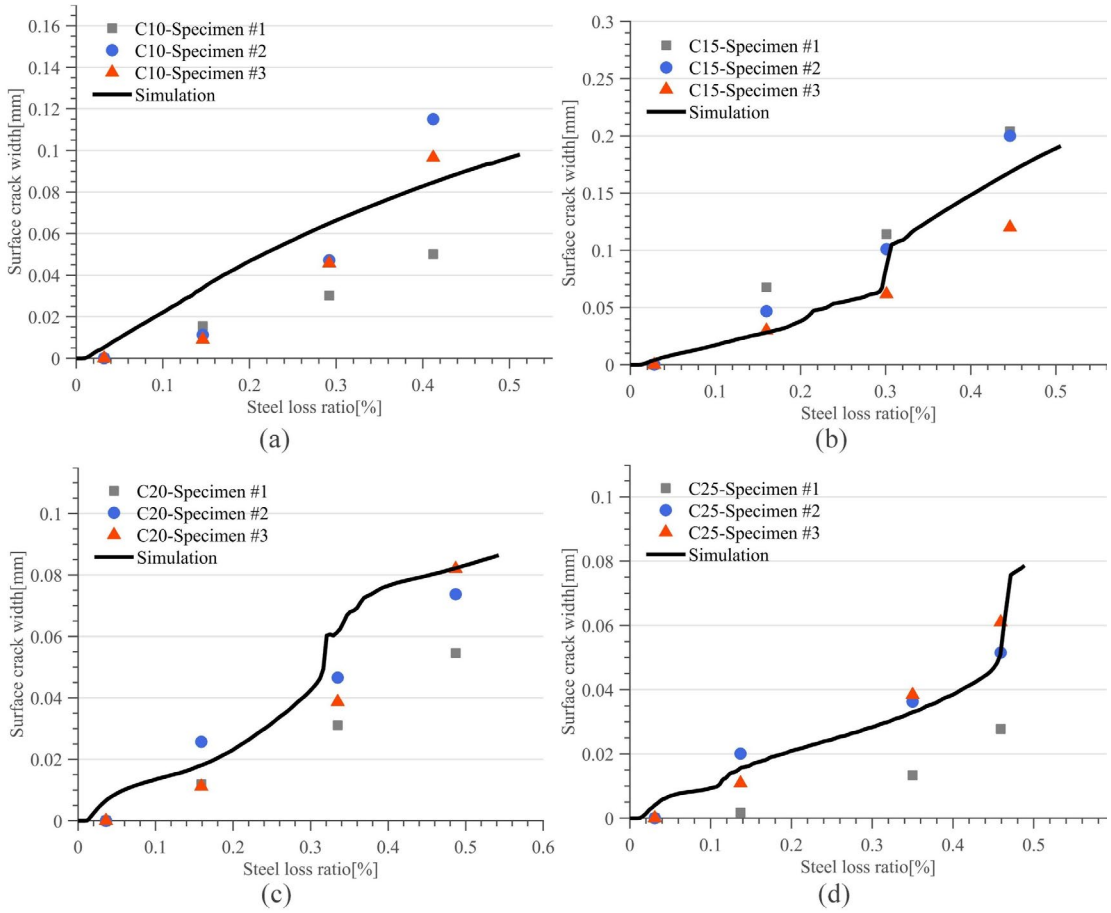

Fig. 9. Predicted and experimental results of the steel loss ration versus surface crack width at different locations: (a) C10; (b) C15; (c) C20; (d) C25.

4. Parametric studies

To investigate the influences of variations in aggregate distribution, cover thickness, humidity and temperature on the entire corrosion process, a 2-D RC beam with one rebar at the center is considered. The dimensions of the beam and placement of the rebar (12mm diameter) are depicted in Fig. 10. The meso-scale model is explicitly considered for only the top section of the beam, with

aggregates, mortar and the ITZs to reduce the computational cost. Other regions are simulated by using a homogenized model. In all the following simulations, a phase field internal length scale $l_0 = 1.0\text{mm}$ is adopted. Theoretically, an accurate way to assess the serviceability of a RC structure would be to model its loading capacity during corrosion. However, due to the high computational effort, the present study adopted a surface crack width of 0.3mm as the serviceability assessment criterion as suggested by (Hu et al., 2022).

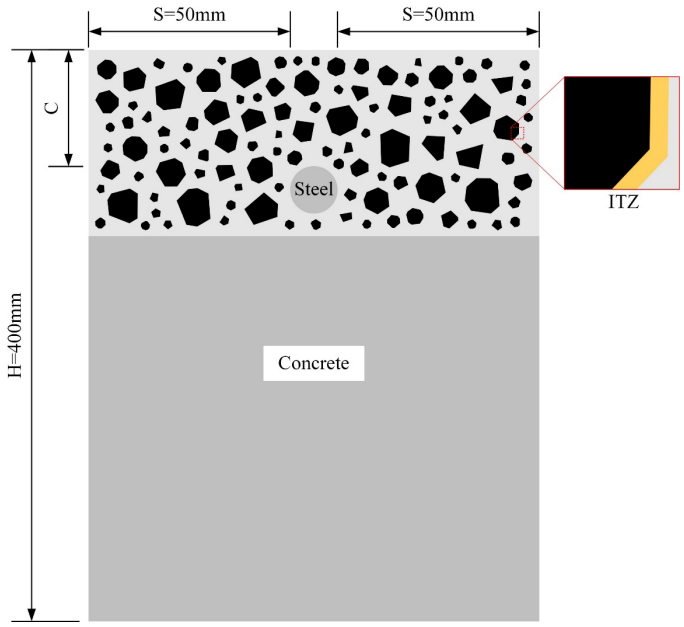

Fig. 10. Meso-scale model of the RC beam with one rebar.

4.1. Influence of aggregate distribution on the corrosion-induced fracture

In order to investigate the influence of the aggregate distribution, 10 random meso-scale models are considered for the entire corrosion process simulation. The concrete cover thickness is $C = 30\text{mm}$. As suggested by Muthulingam and Rao (2014), the chloride concentration at the concrete surface is set to be $C_{cl}^{s}(t) = 0.12t^{0.54}$. The oxygen concentration dissolved in the surface pore solution is assumed to be $0.268\ \text{mol/m}^3$ (Cao et al., 2013). The environmental temperature and humidity are 23°C and 70%, respectively.

Fig. 11 shows the predicted crack patterns of the ten random meso-scale models. The typical crack patterns for different cases are quite similar, containing two side cracks and one vertical crack.

As shown in the figure, side cracks initiate from the rebar surface due to the tensile stress state and then propagate to the lateral surfaces of the beam. On the contrary, the vertical cracks initiate from the top of the beam and propagate to the rebar (Xi and Yang, 2017). It can be observed that the specified paths are different and significantly affected by the aggregate locations, thus showing the influence of the aggregate distribution on the crack path. The overall crack patterns of the 10 random meso-scale models are summarized in Fig. 12(a) by solid red lines where the grey areas represent the potential damage areas of the RC beam subjected to corrosion. It can be seen that the potential cracking area agrees well with the experimental results (Amalia et al., 2018).

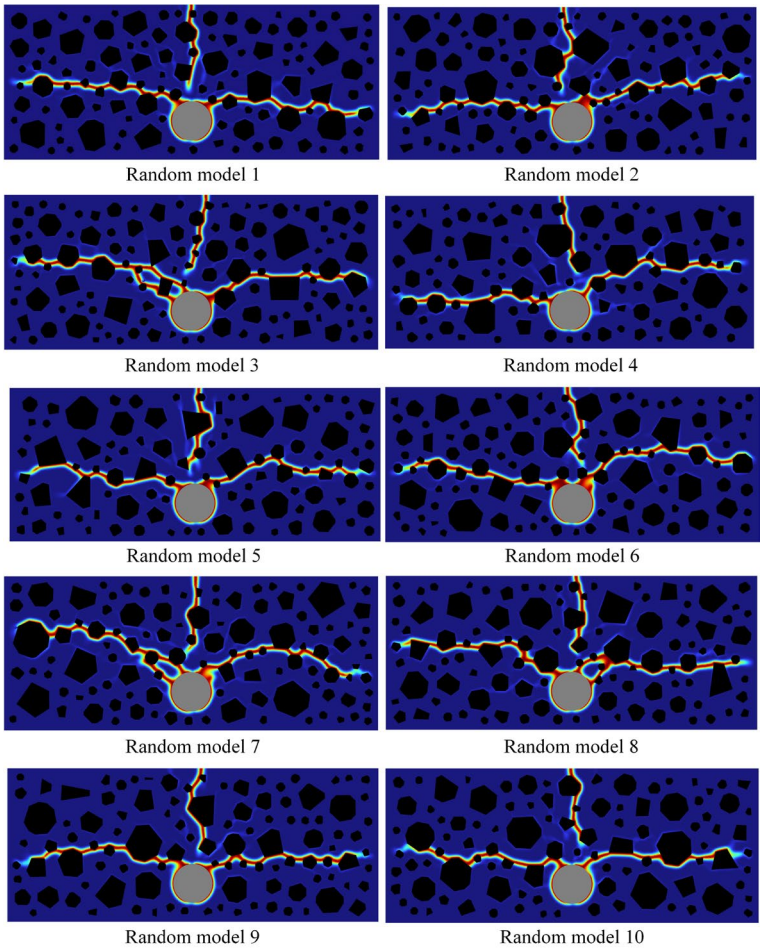

Fig. 11. Crack patterns of 10 random meso-scale models at critical crack width.

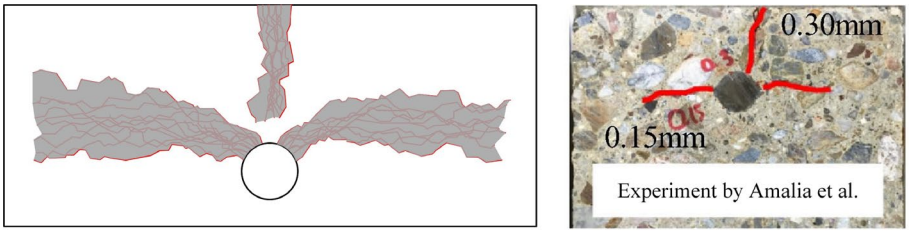

Fig. 12. Summary of crack patterns from (a) different random mesoscale models and (b) experimental data (Amalia et al., 2018).

The corrosion depth (dissolved iron) $p(\boldsymbol{x},t)$ and the rust expansion $u_{rust}(\boldsymbol{x},t)$ for different random models when the surface cracks reach the critical crack width are shown in Fig. 11, where both $p(\boldsymbol{x},t)$ and $u_{rust}(\boldsymbol{x},t)$ are scaled up by 10 times for a better illustration. It seems that the depassivation initiates first from the top surface of the rebar, resulting in localized corrosion. The corrosion propagates towards the bottom, and micro-cell corrosion dominates the corrosion process, resulting in homogenous corrosion of the entire rebar. Therefore, the ultimate corrosion shape will be like a semi-ellipse band. The figure shows that the aggregate distribution has a minor influence on the corrosion depth (represented by red areas) and the rust accumulation (represented by yellow areas). Fig. 14 shows the average corrosion densities of different aggregate distributions when the critical surface crack width is reached. It can be observed that the average corrosion densities of the 10 random models varies with the aggregate distribution, which is consistent with the shapes of the corroded rebars, as depicted in Fig. 13.

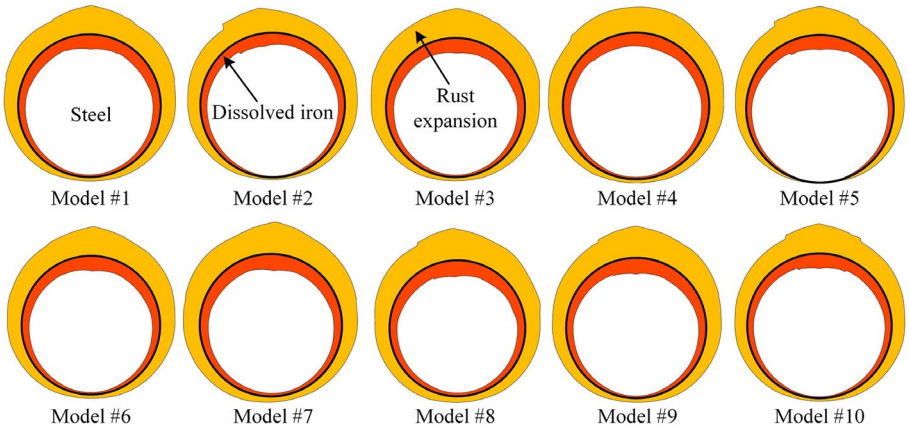

Fig. 13. Shape of corroded rebars for 10 random meso-scale models at critical crack width. (Deformation scale factor: 10)

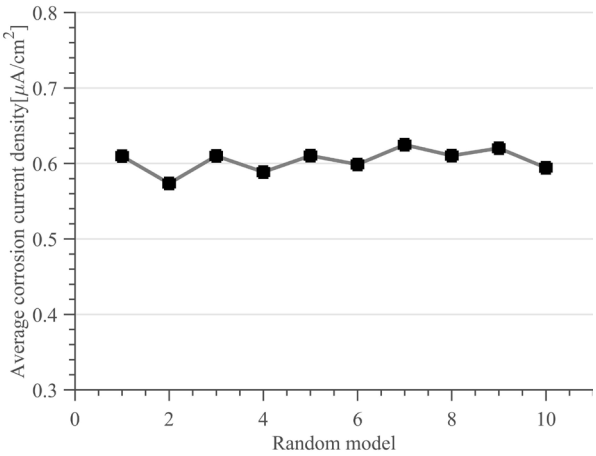

Fig. 14. Average corrosion current densities for different random meso-scale models at critical crack width.

Fig. 15 shows the time-surface crack width curves of the different aggregate distributions. It can be seen that all the curves show first a rapid increase until $0.07\text{mm} - 0.1\text{mm}$. After that, the curves become flatter, showing a nearly bilinear form. The rapid increase in the surface crack width is caused by the stress transfer within the concrete cover, and a larger cover depth will result in wider surface crack, especially when the rust accumulation is localized on the top area of the rebar. This size effect of the concrete cover will be carefully discussed in the following section. For the surface crack width curves depicted in Fig. 15, it can be seen that for different cases the surface cracks initiate between the 11.55th and 13.2th year, and reach the critical crack width 0.3 mm between 20.12th and 24.51th year. In most cases, the average time from crack initiation to reaching its critical width is about 9.94 years.

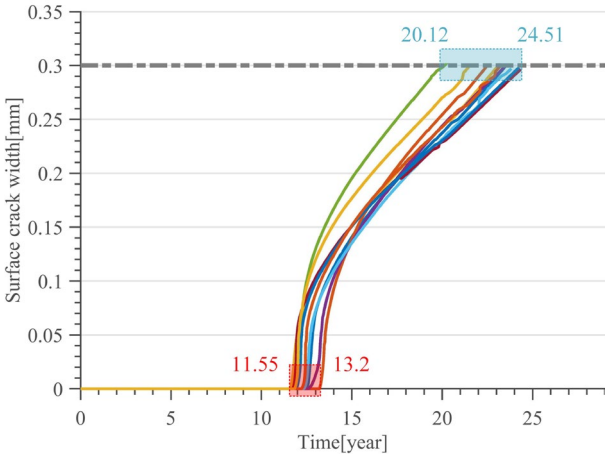

Fig. 15. Time-surface crack width curves of 10 random meso-scale models.

609 4.2. Influence of cover thickness on the corrosion-induced fracture

610 In this section, three different cases, i.e., $C = 20\text{mm}$, $C = 30\text{mm}$ and $C = 40\text{mm}$, are considered
611 to investigate the influence of the concrete cover thickness C on the corrosion process. The
612 aggregate distribution of the thicker cover case is constructed based on that of the thinner cover,
613 ensuring a relatively identical aggregate distribution around the rebar as shown in Fig. 16. Fig. 16
614 shows the crack patterns for different cover thicknesses, which look quite similar in terms of both
615 vertical and side cracks. However, for $C = 40\text{mm}$, Fig. 16 shows that there are two additional
616 smaller side cracks around the rebar. This may be because thicker cover thickness leads to higher
617 expansive pressure, resulting in more cracks to release this constraint.
618

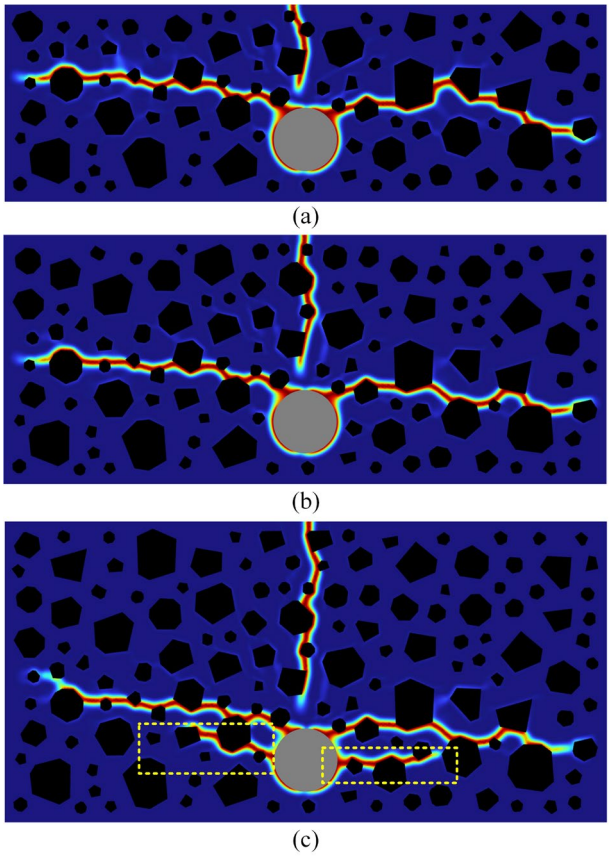

619
620 Fig. 16. Crack patterns for different cover thicknesses at critical surface width: (a) C=20mm; (b)
621 C=30mm; (c) C=40mm.
622

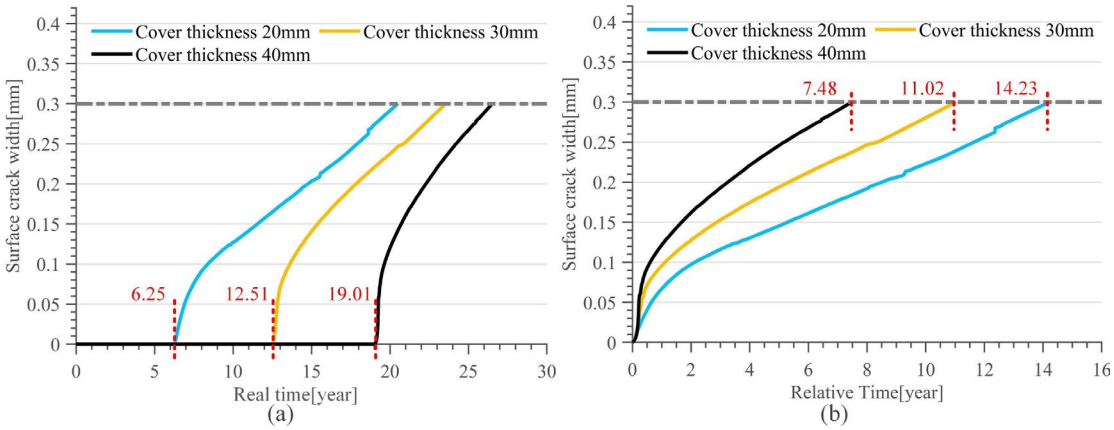

Fig. 17. Time-surface crack width curves for different cover thicknesses: (a) real time; (b) time relative to surface crack initiation.

Fig. 17 shows the relationships between the exposed time and the surface crack width for different cover thicknesses. For 20 mm, 30 mm and 40 mm cases, the corresponding surface cracks appear after 6.25, 12.51 and 19.01 years, indicating a significant influence of cover thickness on the corrosion. Fig. 17(b) shows the relationship between relative time, the time after the surface crack initiation, and the surface crack width. The time from surface crack initiation to reaching the critical width is 7.48 years, 11.02 years, and 14.23 years for cover thickness $C = 20\text{mm}$, $C = 30\text{mm}$ and $C = 40\text{mm}$. In summary, the corrosion analyses show that a thicker concrete cover can delay the time of surface crack initiation. On the other hand, it may accelerate the corresponding crack opening rate and result in a lower load-bearing capacity of the RC structure given the same structural dimensions. Therefore, an optimal cover thickness under specified loading and environmental conditions may be determined to balance the safety and serviceability requirements by combing the proposed modeling framework with an appropriate optimization algorithm.

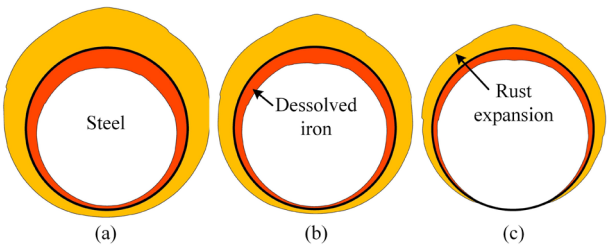

Fig. 18. Shape of the corroded rebars at critical crack width for the cover thickness of (a) 20mm, (b) 30mm, and (c) 40mm. (Deformation scale factor: 10)

Fig. 18 shows the shape of the corroded rebars for different cover thicknesses when crack width reaches its critical value. Red and yellow regions represent the dissolved iron and the accumulated rust product, and a deformation scale factor of 10 is adopted for better illustration. It can be clearly observed that when the surface crack reaches the critical width, the corrosion degree (steel loss ratio) for thinner cover thickness is bigger, indicating that the thinner cover thickness case experienced longer corrosion time from crack surface initiation to reaching the critical value. This observation is consistent with the surface crack width curves depicted in Fig. 17.

Fig. 19 shows the relationships between the corrosion current density and the exposure time at different locations on the rebar surface. It can be observed that at $\theta = 0$ and $\theta = \pi/2$, the corrosion current densities show a sharp increase, then decrease gradually. While at location $\theta = \pi$ the corrosion current densities become constant values after sharp increases, indicating that at this time the corrosion process is mainly dominated by the micro-cell corrosion mechanism. In addition, comparisons between different thickness cases show that the steady corrosion current density decreases with the increase of the cover thickness.

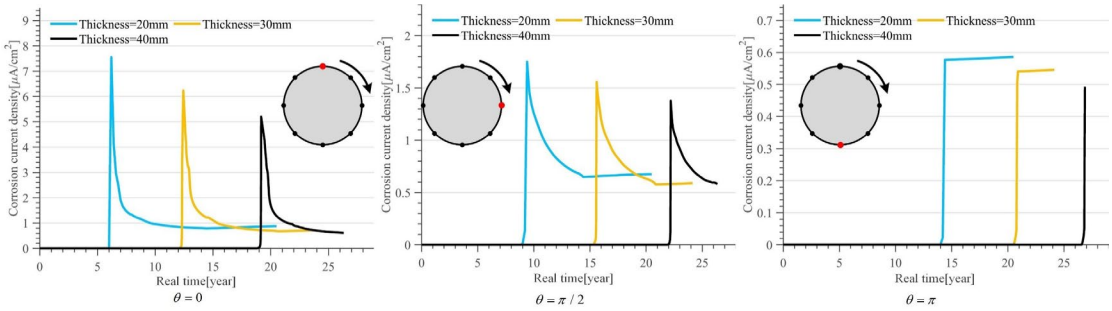

Fig. 19. Corrosion current densities at different locations with different cover thicknesses.

4.3. Influence of relative humidity on the corrosion-induced fracture

Section 2 shows that the relative humidity considerably affects all the mass transport processes, i.e., the transport of moisture, chloride and oxygen. Hence, this section considered three relative humidity cases: 50%, 70% and 90%. It should be noted that the 50% relative humidity is out of the humidity range of the experimental results used for determining the oxygen diffusivity (Eq. (20). However, Eq. (20) is a monolithic function of humidity. It is assuming that it still can reflect some characteristics of the oxygen diffusivity change out of the experimental relative humidity range. Fig.

20 depicts the relationships between the surface crack width and the exposure time of different relative humidity cases. It can be seen that the relative humidity significantly affects the surface crack initiation time. For 50%, 70% and 90% humidity cases, the cracks initiate at the 49.53th year, 12.51th year and 5.48th year. Fig. 20(b) shows that for the lowest relative humidity case (h=50%), the period from surface crack initiation to reaching the critical width is about 2.93 years, much shorter than that of the other cases. And the surface crack width curve of 50% relative humidity is quite different from the other two cases. This may be caused by the highly localized rust accumulation, as shown in Fig. 21(a). It shows that in the case of 50% relative humidity, only about one-quarter of the rebar surface is corroded. In addition, the rust layer has two sharp corners near the corrosion-induced cracks. In contrast, the corrosion for 90% relative humidity is rather uniform, as shown in Fig. 21(c). Because higher humidity leads to bigger diffusion coefficients and higher oxygen access, which will accelerate the depassivation process. The corresponding corrosion current densities for different humidity cases are depicted in Fig. 22. It can be seen that the corrosion current density distributions are consistent with the corrosion shapes shown in Fig. 21.

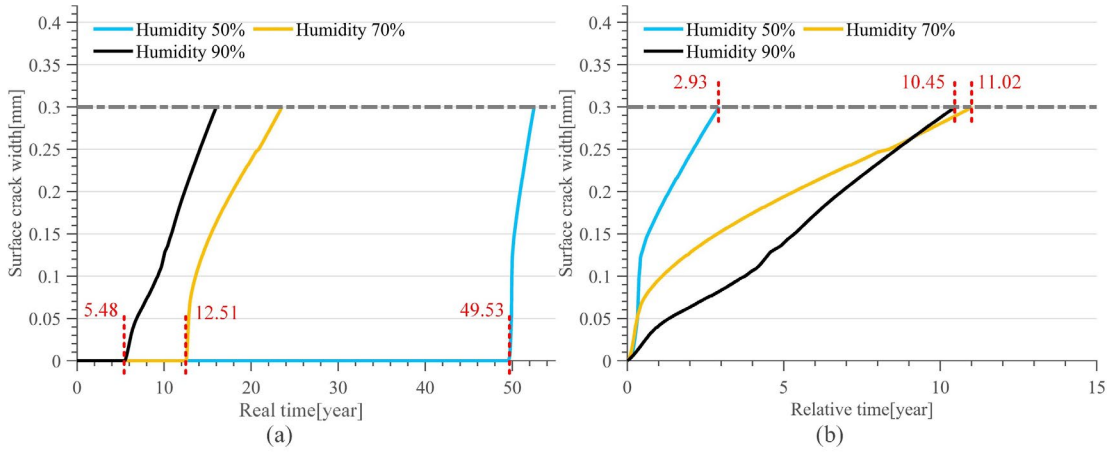

Fig. 20. Time-surface crack width curves for different humidity cases: (a) real time; (b) time relative to surface crack initiation.

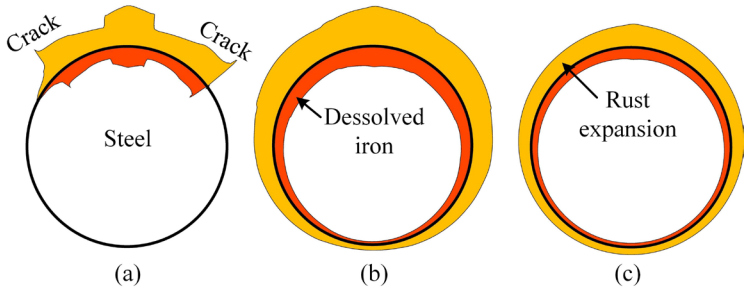

688

689 Fig. 21. Corrosion shapes of the rebars for humidity cases at critical crack width: (a) 50%; (b)
690 70%; (c) 90%. (Deformation scale factor: 10)

691

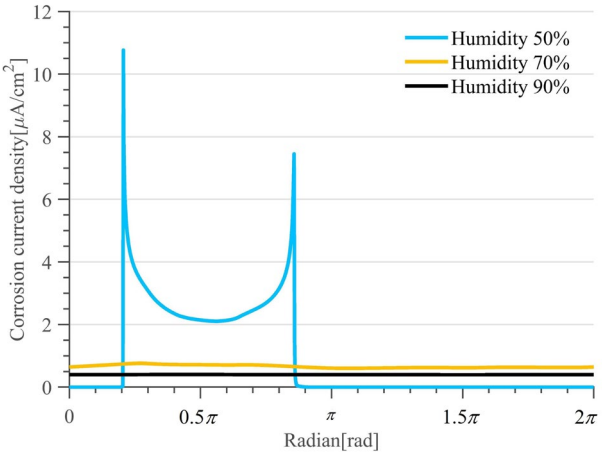

692

693 Fig. 22. Corrosion current densities for different humidity cases at the critical crack width.

694

695 The predicted crack patterns for different humidity cases are depicted in Fig. 23. It can be
696 observed that the crack patterns of 50% and 70% cases are similar to each other. For the 90% case,
697 the crack pattern is very different. It can be seen from Fig. 23(c) that the side cracks are located near
698 the bottom of the rebar, and additional microcracks initiate near the rebar surface. This different
699 crack pattern is actually caused by the relatively uniform corrosion as shown in Fig. 21(c), where
700 the mortar around the rebar is subjected to a relatively uniform hoop stress.

701

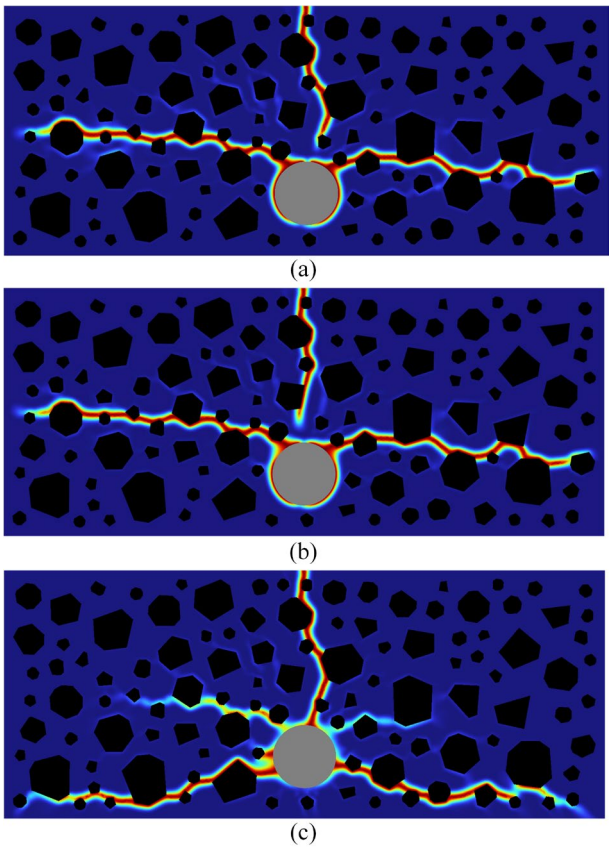

Fig. 23. Crack patterns for different relative humidity cases at the critical crack width: (a) 50%; (b) 70%; (c) 90%.

4.4. Influence of temperature on the corrosion induced fracture

As shown in sections 2 and 2.2, temperature can affect both the mass transport and the electrochemical reactions. In order to investigate the influence of the temperature on the entire corrosion process, three different temperatures were considered, i.e., T=20°C, T=30°C and T=40°C. As suggested by Pour-Ghaz et al. (2009a), the temperature also affects the amount of oxygen that is dissolved in water, and the effect can be evaluated by

$$\ln C_{O_2}^s = -139.344 + \frac{1.575 \times 10^5}{T} - \frac{6.642 \times 10^7}{T^2} + \frac{1.244 \times 10^{10}}{T^3} - \frac{8.622 \times 10^{11}}{T^4} \quad (91)$$

where $C_{O_2}^s$ is the oxygen concentration in the pore solution at the concrete surface (mg/L). Fig. 24 shows the predicted crack patterns and corrosion shapes of different temperatures. It can be observed that the temperature significantly affects the crack patterns and the corrosion shapes. For the cases of T=20°C and T=30°C, the crack patterns are quite similar. For T=40°C two additional radial cracks initiates at the bottom of the rebar surface, behaving more like a uniform corrosion fracture pattern.

The corresponding corrosion shape in Fig. 24 suggests that higher temperature does not necessarily lead to a bigger steel loss ratio.

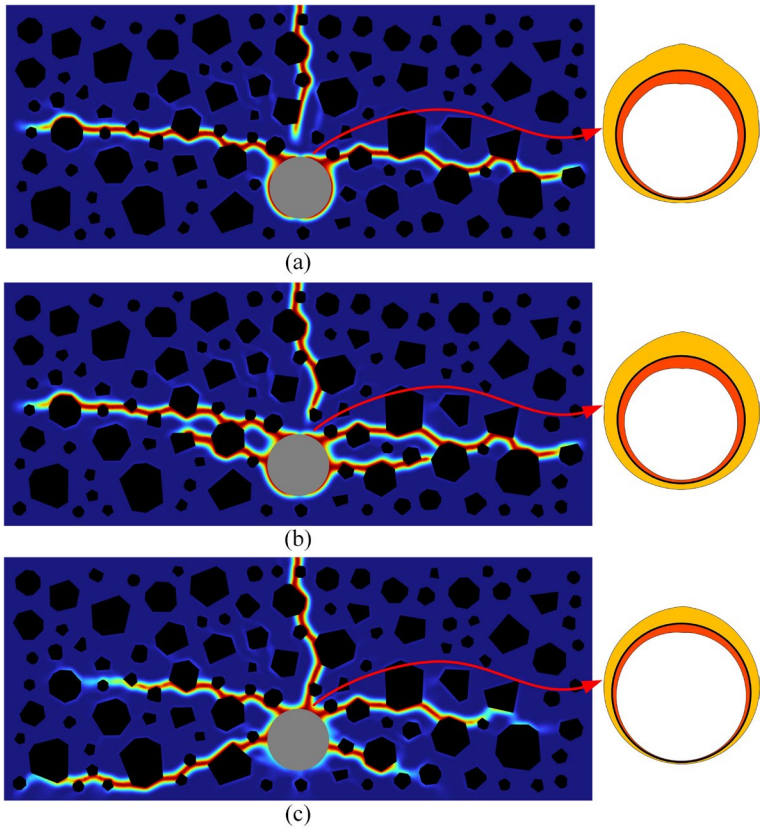

Fig. 24. Crack patterns for different temperatures at the critical crack width: (a) 20ºC; (b) 30ºC; (c) 40ºC.

Fig. 25(a) shows the relationships between the surface crack width and the exposed time of different temperatures. It can be seen that higher temperature can accelerate the onset of the surface cracks, that the surface crack initiation time for 20ºC, 30ºC and 40ºC are 14.2th year, 8.87th year and 5.86th year, respectively. The crack surface width versus relative time curves in Fig. 25(b) shows that it takes longer time to reach the critical crack width in case of a lower temperature. The average corrosion current densities of different temperatures are shown in Fig. 26. It can be clearly observed that the steady corrosion current density increases with the temperature in the current simulation, supporting that the higher temperature leads to less time to reach the critical crack width.

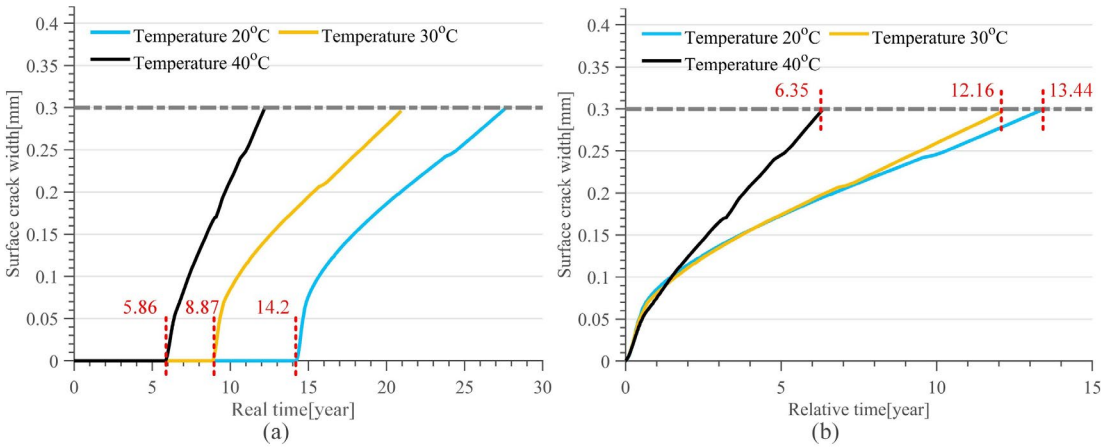

Fig. 25. Time-surface crack width curves for different temperatures: (a) real time; (b) time relative to surface crack initiation.

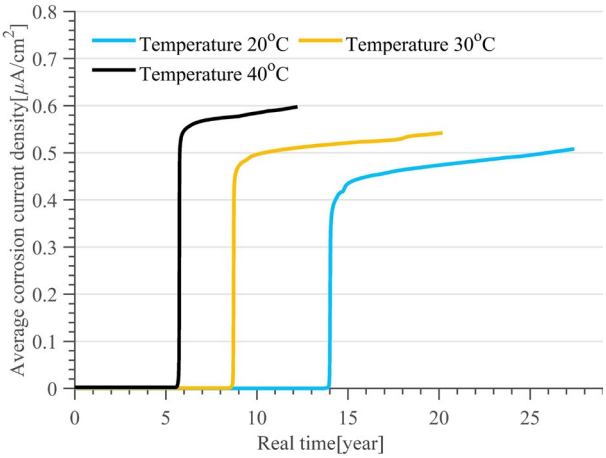

Fig. 26. Average corrosion current curves of different temperatures after surface crack initiation.

5. Conclusions

In this paper, a fully coupled electro-chemo-mechanical phase field method is established to simulate the entire corrosion process of RC structures. In the modeling, the non-mechanical processes (mass transport and electrochemical corrosion) and the mechanical behavior (damage) are coupled together at meso-scale. Modified crack direction-dependent diffusion coefficient tensors are proposed to implement the effect of damage on the transport of moisture, chloride and oxygen in concrete. Experimental results of a RC beam containing four rebars are simulated to verify the proposed method, showing the ability to conduct high-fidelity simulations of corrosion-induced fracture in RC structures. Based on the simulations, the following conclusions can be reached:

(1) The aggregate distribution in concrete significantly influences the mass transport process and the damage evolution, leading to variable crack initiation time and the time required for the crack to reach critical width. However, the major influence is observed in time when the crack reaches the critical width. The simulations show that the time can vary by about 20% with different aggregate distributions.

(2) Thicker concrete cover thickness can delay the onset of surface cracks. However, it will lead to a more rapid increase of the crack width after initiation and a shorter time from surface crack initiation to reaching the critical value.

(3) Higher relative humidity will accelerate the depassivation process, resulting in the early onset of surface cracks. In addition, with the faster depassivation of the rebar surface, the rebar will show a relatively uniform corrosion shape.

(4) The temperature has a clear influence on the corrosion shape of the rebar as well as the corresponding crack pattern. Higher temperatures can accelerate the initiation and propagation of corrosion on the rebar surface.

Acknowledgements

This research was supported by Guangdong Province R&D Plan for Key Areas (Project code: 2019B111107002), the Hong Kong Research Grants Council – Theme-based Research Scheme (Project code: T22-502/18-R), and The Hong Kong Polytechnic University through the Post-doctoral Fellowship (Project code: 1-W21R) and the Research Institute for Sustainable Urban Development (No.1-BBWE).

References

Aldea, C.-M., Ghandehari, M., Shah, S. P. and Karr, A. (2000) 'Estimation of water flow through cracked concrete under load', *Materials Journal,* 97(5), pp. 567-575.

Alonso, C., Andrade, C., Rodriguez, J. and Diez, J. M. (1998) 'Factors controlling cracking of concrete affected by reinforcement corrosion', *Materials and Structures,* 31(7), pp. 435-441.

Amalia, Z., Qiao, D., Nakamura, H., Miura, T. and Yamamoto, Y. (2018) 'Development of simulation method of concrete cracking behavior and corrosion products movement due to rebar corrosion', *Construction and Building Materials,* 190, pp. 560-572.

Ambati, M., Gerasimov, T. and De Lorenzis, L. (2015a) 'Phase-field modeling of ductile fracture', *Computational Mechanics,* 55(5), pp. 1017-1040.

Ambati, M., Gerasimov, T. and De Lorenzis, L. (2015b) 'A review on phase-field models of brittle

781 fracture and a new fast hybrid formulation', *Computational Mechanics,* 55(2), pp. 383-405.
782 Andrade, C., Alonso, C. and Molina, F. (1993) 'Cover cracking as a function of bar corrosion: Part I-
783 Experimental test', *Materials and Structures,* 26(8), pp. 453-464.
784 Angst, U., Elsener, B., Larsen, C. K. and Vennesland, Ø. (2009) 'Critical chloride content in reinforced
785 concrete—A review', *Cement and Concrete Research,* 39(12), pp. 1122-1138.
786 Baroghel-Bouny, V. (2007) 'Water vapour sorption experiments on hardened cementitious materials. Part
787 II: Essential tool for assessment of transport properties and for durability prediction', *Cement*
788 *and Concrete Research,* 37(3), pp. 438-454.
789 Bažant, Z. and Najjar, L. (1972) 'Nonlinear water diffusion in nonsaturated concrete', *Matériaux et*
790 *Construction,* 5(1), pp. 3-20.
791 Bear, J. and Bachmat, Y. (2012) *Introduction to modeling of transport phenomena in porous media.*
792 Springer Science & Business Media.
793 Borden, M. J. (2012) *Isogeometric analysis of phase-field models for dynamic brittle and ductile fracture.*
794 PhD dissertation, The University of Texas at Austin.
795 Bourdin, B., Francfort, G. A. and Marigo, J.-J. (2000) 'Numerical experiments in revisited brittle fracture',
796 *Journal of the Mechanics and Physics of Solids,* 48(4), pp. 797-826.
797 Bourdin, B., Larsen, C. J. and Richardson, C. L. (2011) 'A time-discrete model for dynamic fracture
798 based on crack regularization', *International Journal of Fracture,* 168(2), pp. 133-143.
799 Cabrera, J. G. (1996) 'Deterioration of concrete due to reinforcement steel corrosion', *Cement and*
800 *Concrete Composites,* 18(1), pp. 47-59.
801 Cao, C. and Cheung, M. M. (2014) 'Non-uniform rust expansion for chloride-induced pitting corrosion
802 in RC structures', *Construction and Building Materials,* 51, pp. 75-81.
803 Cao, C., Cheung, M. M. and Chan, B. Y. (2013) 'Modelling of interaction between corrosion-induced
804 concrete cover crack and steel corrosion rate', *Corrosion Science,* 69, pp. 97-109.
805 Castel, A., François, R. and Arliguie, G. (2000) 'Mechanical behaviour of corroded reinforced concrete
806 beams—Part 1: Experimental study of corroded beams', *Materials and Structures,* 33(9), pp.
807 539-544.
808 Chauhan, A. and Sharma, U. K. (2021) 'Crack propagation in reinforced concrete exposed to non-uniform
809 corrosion under real climate', *Engineering Fracture Mechanics,* 248, pp. 107719.
810 Chen, A., Pan, Z. and Ma, R. (2018) 'Mesoscopic simulation of steel rebar corrosion process in concrete
811 and its damage to concrete cover', *Bridge Design, Assessment and Monitoring*: Routledge, pp.
812 62-77.
813 Christensen, R. (1979) 'Mechanics of Composite Materials Wiley', *New York*, pp. 75.
814 Code, P. (2005) 'Eurocode 2: design of concrete structures', *British Standard Institution, London*.
815 Contrafatto, L., Cuomo, M. and Gazzo, S. (2016) 'A concrete homogenisation technique at meso-scale
816 level accounting for damaging behaviour of cement paste and aggregates', *Computers &*
817 *Structures,* 173, pp. 1-18.
818 Daian, J.-F. (1988) 'Condensation and isothermal water transfer in cement mortar Part I—Pore size
819 distribution, equilibrium water condensation and imbibition', *Transport in Porous Media,* 3, pp.
820 563-589.
821 de Burgh, J. M., Foster, S. J. and Valipour, H. R. (2016) 'Prediction of water vapour sorption isotherms
822 and microstructure of hardened Portland cement pastes', *Cement and Concrete Research,* 81, pp.
823 134-150.
824 Djerbi, A., Bonnet, S., Khelidj, A. and Baroghel-Bouny, V. (2008) 'Influence of traversing crack on

825 chloride diffusion into concrete', *Cement and Concrete Research,* 38(6), pp. 877-883.
826 Du, X., Jin, L. and Zhang, R. (2014) 'Modeling the cracking of cover concrete due to non-uniform
827 corrosion of reinforcement', *Corrosion Science,* 89, pp. 189-202.
828 Duan, A., Dai, J.-G. and Jin, W.-L. (2015) 'Probabilistic approach for durability design of concrete
829 structures in marine environments', *Journal of Materials in Civil Engineering,* 27(2), pp.
830 A4014007.
831 Fischer, C. (2012) 'Auswirkungen der Bewehrungskorrosion auf den Verbund zwischen Stahl und Beton'.
832 Francfort, G. A. and Marigo, J.-J. (1998) 'Revisiting brittle fracture as an energy minimization problem',
833 *Journal of the Mechanics and Physics of Solids,* 46(8), pp. 1319-1342.
834 Geng, O., Yuan, Y., Zhu, H. and Li, F. (2006) 'Experimental study on diffusion coefficient of oxygen in
835 concrete', *Journal of Southeast University (Natural science edition),* 36, pp. 191-194.
836 Hu, X., Xu, H., Xi, X., Zhang, P. and Yang, S. (2022) 'Meso-scale phase field modelling of reinforced
837 concrete structures subjected to corrosion of multiple reinforcements', *Construction and*
838 *Building Materials,* 321, pp. 126376.
839 Huang, Q., Jiang, Z., Gu, X., Zhang, W. and Guo, B. (2015a) 'Numerical simulation of moisture transport
840 in concrete based on a pore size distribution model', *Cement and Concrete Research,* 67, pp. 31-
841 43.
842 Huang, Y., Yang, Z., Chen, X. and Liu, G. (2016) 'Monte Carlo simulations of meso-scale dynamic
843 compressive behavior of concrete based on X-ray computed tomography images', *International*
844 *Journal of Impact Engineering,* 97, pp. 102-115.
845 Huang, Y., Yang, Z., Ren, W., Liu, G. and Zhang, C. (2015b) '3D meso-scale fracture modelling and
846 validation of concrete based on in-situ X-ray Computed Tomography images using damage
847 plasticity model', *International Journal of Solids and Structures,* 67, pp. 340-352.
848 Ishida, T., Maekawa, K. and Kishi, T. (2007) 'Enhanced modeling of moisture equilibrium and transport
849 in cementitious materials under arbitrary temperature and relative humidity history', *Cement*
850 *and Concrete Research,* 37(4), pp. 565-578.
851 Jaffer, S. J. and Hansson, C. M. (2009) 'Chloride-induced corrosion products of steel in cracked-concrete
852 subjected to different loading conditions', *Cement and Concrete Research,* 39(2), pp. 116-125.
853 Jang, B. S. and Oh, B. H. (2010) 'Effects of non-uniform corrosion on the cracking and service life of
854 reinforced concrete structures', *Cement and Concrete Research,* 40(9), pp. 1441-1450.
855 Jiang, Z., Xi, Y., Gu, X., Huang, Q. and Zhang, W. (2019) 'Modelling of water vapour sorption hysteresis
856 of cement-based materials based on pore size distribution', *Cement and Concrete Research,* 115,
857 pp. 8-19.
858 Li, Y.-Q., Chen, J.-F., Yang, Z.-J., Esmaeeli, E., Sha, W. and Huang, Y.-J. (2021) 'Effects of concrete
859 heterogeneity on FRP-concrete bond behaviour: Experimental and mesoscale numerical studies',
860 *Composite Structures,* 275, pp. 114436.
861 López, C. M., Carol, I. and Aguado, A. (2008) 'Meso-structural study of concrete fracture using interface
862 elements. II: compression, biaxial and Brazilian test', *Materials and Structures,* 41(3), pp. 601-
863 620.
864 Lu, X., Teng, J., Ye, L. and Jiang, J. (2005) 'Bond–slip models for FRP sheets/plates bonded to concrete',
865 *Engineering Structures,* 27(6), pp. 920-937.
866 Luping, T. and Nilsson, L.-O. (1993) 'Chloride binding capacity and binding isotherms of OPC pastes
867 and mortars', *Cement and Concrete Research,* 23(2), pp. 247-253.
868 Maekawa, K. (2008) *Multi-scale modeling of structural concrete.* Crc Press.

869 Martın-Pérez, B., Pantazopoulou, S. J. and Thomas, M. (2001) 'Numerical solution of mass transport
870 equations in concrete structures', *Computers & Structures,* 79(13), pp. 1251-1264.
871 Miehe, C., Hofacker, M., Schänzel, L.-M. and Aldakheel, F. (2015) 'Phase field modeling of fracture in
872 multi-physics problems. Part II. Coupled brittle-to-ductile failure criteria and crack propagation
873 in thermo-elastic–plastic solids', *Computer Methods in Applied Mechanics and Engineering,*
874 294, pp. 486-522.
875 Miehe, C., Welschinger, F. and Hofacker, M. (2010) 'Thermodynamically consistent phase-field models
876 of fracture: Variational principles and multi-field FE implementations', *International Journal*
877 *for Numerical Methods in Engineering,* 83(10), pp. 1273-1311.
878 Mori, T. and Tanaka, K. (1973) 'Average stress in matrix and average elastic energy of materials with
879 misfitting inclusions', *Acta Metallurgica,* 21(5), pp. 571-574.
880 Muthulingam, S. and Rao, B. (2014) 'Non-uniform time-to-corrosion initiation in steel reinforced
881 concrete under chloride environment', *Corrosion Science,* 82, pp. 304-315.
882 Nagai, K., Sato, Y. and Ueda, T. (2005) 'Mesoscopic simulation of failure of mortar and concrete by 3D
883 RBSM', *Journal of Advanced Concrete Technology,* 3(3), pp. 385-402.
884 Ožbolt, J., Balabanić, G. and Kušter, M. (2011) '3D Numerical modelling of steel corrosion in concrete
885 structures', *Corrosion Science,* 53(12), pp. 4166-4177.
886 Ožbolt, J., Balabanić, G., Periškić, G. and Kušter, M. (2010) 'Modelling the effect of damage on transport
887 processes in concrete', *Construction and Building Materials,* 24(9), pp. 1638-1648.
888 Pinson, M. B., Masoero, E., Bonnaud, P. A., Manzano, H., Ji, Q., Yip, S., Thomas, J. J., Bazant, M. Z.,
889 Van Vliet, K. J. and Jennings, H. M. (2015) 'Hysteresis from multiscale porosity: modeling
890 water sorption and shrinkage in cement paste', *Physical Review Applied,* 3(6), pp. 064009.
891 Pour-Ghaz, M., Isgor, O. B. and Ghods, P. (2009a) 'The effect of temperature on the corrosion of steel in
892 concrete. Part 1: Simulated polarization resistance tests and model development', *Corrosion*
893 *Science,* 51(2), pp. 415-425.
894 Pour-Ghaz, M., Isgor, O. B. and Ghods, P. (2009b) 'The effect of temperature on the corrosion of steel in
895 concrete. Part 2: Model verification and parametric study', *Corrosion Science,* 51(2), pp. 426-
896 433.
897 Qiu, Q. and Dai, J. G. (2021) 'Meso-scale modeling of chloride diffusivity in mortar subjected to
898 corrosion-induced cracking', *Computer-Aided Civil and Infrastructure Engineering,* 36(5), pp.
899 602-619.
900 Quintanas-Corominas, A., Reinoso, J., Casoni, E., Turon, A. and Mayugo, J. (2019) 'A phase field
901 approach to simulate intralaminar and translaminar fracture in long fiber composite materials',
902 *Composite Structures,* 220, pp. 899-911.
903 Ranaivomanana, H., Verdier, J., Sellier, A. and Bourbon, X. (2011) 'Toward a better comprehension and
904 modeling of hysteresis cycles in the water sorption–desorption process for cement based
905 materials', *Cement and Concrete Research,* 41(8), pp. 817-827.
906 Saetta, A. V., Scotta, R. V. and Vitaliani, R. V. (1993) 'Analysis of chloride diffusion into partially
907 saturated concrete', *Materials Journal,* 90(5), pp. 441-451.
908 Šavija, B., Luković, M., Pacheco, J. and Schlangen, E. (2013) 'Cracking of the concrete cover due to
909 reinforcement corrosion: A two-dimensional lattice model study', *Construction and Building*
910 *Materials,* 44, pp. 626-638.
911 Shafikhani, M. and Chidiac, S. (2019) 'Quantification of concrete chloride diffusion coefficient–A critical
912 review', *Cement and Concrete Composites,* 99, pp. 225-250.

913 Sideris, K., Manita, P. and Sideris, K. (2004) 'Estimation of ultimate modulus of elasticity and Poisson
914 ratio of normal concrete', *Cement and Concrete Composites,* 26(6), pp. 623-631.
915 Suda, K., Misra, S. and Motohashi, K. (1993) 'Corrosion products of reinforcing bars embedded in
916 concrete', *Corrosion Science,* 35(5-8), pp. 1543-1549.
917 Tran, K. K., Nakamura, H., Kawamura, K. and Kunieda, M. (2011) 'Analysis of crack propagation due
918 to rebar corrosion using RBSM', *Cement and Concrete Composites,* 33(9), pp. 906-917.
919 Van Genuchten, M. T. (1980) 'A closed-form equation for predicting the hydraulic conductivity of
920 unsaturated soils', *Soil science society of America Journal,* 44(5), pp. 892-898.
921 Wang, K., Jansen, D. C., Shah, S. P. and Karr, A. F. (1997) 'Permeability study of cracked concrete',
922 *Cement and concrete research,* 27(3), pp. 381-393.
923 Wei, C., Wojnar, C. S. and Wu, C. (2021) 'Hydro-chemo-mechanical phase field formulation for corrosion
924 induced cracking in reinforced concrete', *Cement and Concrete Research,* 144, pp. 106404.
925 Wong, H., Zhao, Y., Karimi, A., Buenfeld, N. and Jin, W. (2010) 'On the penetration of corrosion products
926 from reinforcing steel into concrete due to chloride-induced corrosion', *Corrosion Science,*
927 52(7), pp. 2469-2480.
928 Wu, J.-Y. (2017) 'A unified phase-field theory for the mechanics of damage and quasi-brittle failure',
929 *Journal of the Mechanics and Physics of Solids,* 103, pp. 72-99.
930 Xi, X. and Yang, S. (2017) 'Time to surface cracking and crack width of reinforced concrete structures
931 under corrosion of multiple rebars', *Construction and Building Materials,* 155, pp. 114-125.
932 Xi, X., Yang, S. and Li, C.-Q. (2018a) 'A non-uniform corrosion model and meso-scale fracture modelling
933 of concrete', *Cement and Concrete Research,* 108, pp. 87-102.
934 Xi, X., Yang, S., Li, C.-Q., Cai, M., Hu, X. and Shipton, Z. K. (2018b) 'Meso-scale mixed-mode fracture
935 modelling of reinforced concrete structures subjected to non-uniform corrosion', *Engineering*
936 *Fracture Mechanics,* 199, pp. 114-130.
937 Xi, Y. and Bažant, Z. P. (1999) 'Modeling chloride penetration in saturated concrete', *Journal of Materials*
938 *in Civil Engineering,* 11(1), pp. 58-65.
939 Xi, Y., Bažant, Z. P. and Jennings, H. M. (1994a) 'Moisture diffusion in cementitious materials adsorption
940 isotherms', *Advanced Cement Based Materials,* 1(6), pp. 248-257.
941 Xi, Y., Bažant, Z. P., Molina, L. and Jennings, H. M. (1994b) 'Moisture diffusion in cementitious
942 materials moisture capacity and diffusivity', *Advanced Cement Based Materials,* 1(6), pp. 258-
943 266.
944 Ye, H., Jin, N., Fu, C. and Jin, X. (2017) 'Rust distribution and corrosion-induced cracking patterns of
945 corner-located rebar in concrete cover', *Construction and Building Materials,* 156, pp. 684-691.
946 Yu, B., Liu, J. and Li, B. (2017) 'Improved numerical model for steel reinforcement corrosion in concrete
947 considering influences of temperature and relative humidity', *Construction and Building*
948 *Materials,* 142, pp. 175-186.
949 Zhang, J., Ling, X. and Guan, Z. (2017) 'Finite element modeling of concrete cover crack propagation
950 due to non-uniform corrosion of reinforcement', *Construction and Building Materials,* 132, pp.
951 487-499.
952 Zhang, P., Hu, X., Bui, T. Q. and Yao, W. (2019a) 'Phase field modeling of fracture in fiber reinforced
953 composite laminate', *International Journal of Mechanical Sciences,* 161, pp. 105008.
954 Zhang, P., Hu, X., Yang, S. and Yao, W. (2019b) 'Modelling progressive failure in multi-phase materials
955 using a phase field method', *Engineering Fracture Mechanics,* 209, pp. 105-124.
956 Zhang, P., Yao, W., Hu, X. and Bui, T. Q. (2021) 'An explicit phase field model for progressive tensile

957 failure of composites', *Engineering Fracture Mechanics,* 241, pp. 107371.
958 Zhao, Y., Karimi, A. R., Wong, H. S., Hu, B., Buenfeld, N. R. and Jin, W. (2011) 'Comparison of uniform
959 and non-uniform corrosion induced damage in reinforced concrete based on a Gaussian
960 description of the corrosion layer', *Corrosion Science,* 53(9), pp. 2803-2814.
961 Zhou, R., Song, Z. and Lu, Y. (2017) '3D mesoscale finite element modelling of concrete', *Computers &*
962 *Structures,* 192, pp. 96-113.
963 Zhu, X. and Zi, G. (2017) 'A 2D mechano-chemical model for the simulation of reinforcement corrosion
964 and concrete damage', *Construction and Building Materials,* 137, pp. 330-344.
965